



1 How can mountaintop CO₂ observations be used to constrain regional 2 carbon fluxes?

3 John C. Lin¹, Derek V. Mallia¹, Dien Wu¹, Britton B. Stephens²
4

5 ¹Department of Atmospheric Sciences, University of Utah, Salt Lake City, Utah 84112, USA

6 ²Earth Observing Laboratory, National Center for Atmospheric Research, Boulder, Colorado
7 80301, USA

8 *Correspondence to:* John C. Lin (John.Lin@utah.edu)
9

10 Manuscript Submitted to Atmospheric Chemistry and Physics

11 **Abstract.**

12 Despite the need for researchers to understand terrestrial biospheric carbon fluxes
13 to account for carbon cycle feedbacks and predict future CO₂ concentrations, knowledge
14 of these fluxes at the regional scale remains poor. This is particularly true in
15 mountainous areas, where complex meteorology and lack of observations lead to large
16 uncertainties in carbon fluxes. Yet mountainous regions are often where significant
17 forest cover and biomass are found—i.e., areas that have the potential to serve as carbon
18 sinks. As CO₂ observations are carried out in mountainous areas, it is imperative that
19 they are properly interpreted to yield information about carbon fluxes. In this paper, we
20 present CO₂ observations at 3 sites in the mountains of the Western U.S., along with
21 atmospheric simulations that attempt to extract information about biospheric carbon
22 fluxes from the CO₂ observations, with emphasis on the observed and simulated diurnal
23 cycles of CO₂. We show that atmospheric models can systematically simulate the wrong
24 diurnal cycle and significantly misinterpret the CO₂ observations, due to erroneous
25 atmospheric flows as a result of terrain that is misrepresented in the model. This problem
26 depends on the selected vertical level in the model and are exacerbated as the spatial
27 resolution is degraded, and our results indicate that a fine grid spacing of ~4 km or less
28 may be needed to simulate a realistic diurnal cycle of CO₂ for sites on top of the steep
29 mountains examined here in the American Rockies. In the absence of higher resolution
30 models, we recommend coarse-scale models to focus on assimilating afternoon CO₂
31 observations on mountaintop sites over the continent to avoid misrepresentations of
32 nocturnal transport and influence.

33 **1. Introduction**

34 Scientific consensus among climate scientists points to carbon dioxide (CO₂) as
35 the main greenhouse gas leading to climate change (IPCC, 2014). Therefore, a strong
36 need exists to quantify and understand global carbon fluxes, among which the terrestrial
37 biospheric component is the most dynamic, potentially even reversing signs on an annual
38 basis from year to year (Le Quéré et al., 2015; Sarmiento et al., 2010). Yet quantifying
39 and predicting terrestrial biospheric carbon fluxes continue to pose a challenge to
40 researchers, as seen in the large divergence between models in projections of biospheric
41 fluxes into the future (Cox et al., 2000; Friedlingstein et al., 2003; Arora et al., 2013) as
42 well as in hindcast mode, particularly at the regional scale (Sarmiento et al.,
43 2010; Stephens et al., 2007; Fisher et al., 2014).



44 Because hills and mountains cover almost 70% of the Earth's land surface
45 (Rotach et al., 2008), it is imperative to quantify and understand carbon fluxes over
46 "complex terrain". Case in point is the Western U.S., where significant amounts of
47 biomass are found above 1000 m elevation (Fig. 1). Similarly, much of the biomass and
48 potential for terrestrial carbon storage in other parts of the world are found in hills or
49 mountains, partly due to the fact that historical deforestation and biomass removal have
50 been most pronounced in easier-to-access, flat regions (Ramankutty and Foley, 1999).

51 van der Molen et al. (2007) simulated CO₂ variability near a Siberian
52 observational site and showed that even modest terrain variations of ~500 m over 200 km
53 could lead to considerable CO₂ gradients. Recently, Rotach et al. (2014) argued that
54 current difficulties to balance the terrestrial carbon budget are due to inability to handle
55 complex terrain. While these authors presented a strong case for the consideration of
56 flows over complex terrain, they did not quantify the implications of neglecting such
57 flows for interpreting CO₂ observations.

58 Despite the importance of regions with complex terrain in regional to global
59 carbon cycling, these areas have hitherto been under-sampled due to logistical difficulties,
60 harsh environmental settings, and violation of flat terrain assumptions in eddy covariance.
61 However, the significance of complex terrain has led to efforts to start closing this gap, in
62 regions such as Europe (Pillai et al., 2011) and the American Rockies ((Schimel et al.,
63 2002); see below).

64 The American Rockies will be the focus region of this study, which attempts to
65 show how CO₂ concentrations in mountain regions can be properly linked, through
66 atmospheric transport, to biospheric fluxes. While the objective of this paper is to use the
67 American Rockies as a case study to illustrate general aspects of interpreting CO₂
68 observations in mountainous regions, several other compelling reasons exist for studying
69 this region. Both models and observations have suggested that significant carbon storage
70 can occur in the American Rockies (Fig.1) (Schimel et al., 2002; Monson et al.,
71 2002; Wharton et al., 2012), albeit this storage is highly sensitive to environmental drivers
72 such as temperature and water availability (Monson et al., 2006; Schwalm et al.,
73 2012; Wharton et al., 2012; Potter et al., 2013) as well as disturbances such as insect
74 infestation (Negron and Popp, 2004) and wildfires (Wiedinmyer and Neff, 2007). These
75 disturbances are also coinciding with rapid population increases in this region (Lang et al.,
76 2008), with concomitant rise in urban CO₂ emissions (Mitchell et al., In Review), urban-
77 wildland interfaces (Mell et al., 2010), and demands for water resources (Reisner,
78 1993; Gollehon and Quinby, 2000).

79 Recently, several research efforts have attempted to improve the understanding of
80 carbon fluxes in the American Rockies. Direct eddy covariance-based measurements of
81 carbon fluxes have been carried out in the mountains (Blanken et al., 2009; Yi et al.,
82 2008); however, the eddy covariance technique characterizes fluxes only over a small
83 area of ~1 km² (Baldocchi et al., 2001) and requires careful attention to potential biases
84 from local advection. Ground-based ecological measurements (Anderegg et al.,
85 2012; Tkacz et al., 2008) yield detailed information regarding the ecosystem, but such
86 observations are also limited in spatial coverage and temporal resolution. Atmospheric
87 CO₂ observations can characterize fluxes over hundreds of km (Gerbig et al., 2009),
88 providing important regional scale constraints. Aircraft-based CO₂ measurements in this
89 region have had some success in characterizing regional scale fluxes (Desai et al., 2011),



90 albeit on a sporadic, campaign-based setting. More significantly, a network of accurate
91 CO₂ observations has been maintained on mountaintops in the Rockies for the past
92 decade (Stephens et al., 2011). These observations have been assimilated by
93 sophisticated global carbon data assimilation systems such as “CarbonTracker” (Peters et
94 al., 2007) to retrieve biospheric carbon fluxes over the mountainous regions and the rest
95 of the globe.

96 Due to the expanding number of CO₂ observations in mountainous areas and the
97 need to understand carbon fluxes in such regions, a strong motivation exists to evaluate
98 existing methods in which CO₂ observations are used in atmospheric models to retrieve
99 carbon fluxes. We specifically adopt the observed diurnal cycle during the summer
100 growing season as a key diagnostic to evaluate models. This is because the diurnal cycle
101 during the growing season, with nighttime respiratory release and daytime photosynthetic
102 drawdown of CO₂, is a prominent feature in the coupling between biospheric fluxes and
103 the atmosphere and one of the dominant modes in the CO₂ time series (Bakwin et al.,
104 1998; Denning et al., 1996). Furthermore, models tend to either use CO₂ data from the
105 nighttime (Keeling et al., 1976) (to sample subsiding air in the mid-troposphere) or from
106 the daytime (during well-mixed conditions), and aspects of the diurnal cycle can provide
107 clues as to whether the model is capturing the link between fluxes and concentrations
108 right at either, both, or neither of these times.

109 The diurnal pattern of CO₂ observed at the Storm Peak Laboratory, Colorado, was
110 examined by one of the first mesoscale modeling studies that investigated the impact of
111 mountain flows on CO₂ concentrations (De Wekker et al., 2009). Although this study
112 adopted an idealized simulation covering only a single day of observations, it nonetheless
113 underscored the role of daytime upslope winds. A common approach is to assimilate
114 mountain observations at night (Peters et al., 2007), favoring subsidence conditions
115 characterizing free tropospheric concentrations and avoiding the need to resolve daytime
116 upslope flows (Keeling et al., 1976).

117 Recently, Brooks et al. (2016) used pseudo-observations to examine the
118 detectability of a regional flux anomaly by three mountaintop CO₂ sites in the American
119 Rockies (including Storm Peak Laboratory). For the atmospheric model they adopted a
120 time-reversed Lagrangian particle dispersion model (LPDM), which yields the
121 “footprint”, or source region, of the observation sites (Lin et al., 2012). Although this
122 study investigated whether the three mountaintop sites could detect signals of ecosystem
123 disturbance, Brooks et al. (2016) did not specifically examine issues related to erroneous
124 atmospheric transport in complex terrain nor compare modeled CO₂ against observed
125 values.

126 In this paper, we will focus on the same 3 mountaintop CO₂ sites in the American
127 Rockies and specifically examine the implications of using nocturnal versus daytime data
128 within models, in light of atmospheric models at various grid spacings—from high
129 resolution regional simulations to coarser global scale simulations. More specifically, we
130 will drive a time-reversed LPDM with various meteorological fields and receptor heights.
131 We will probe the implications on the footprint, transport, and the resulting CO₂
132 concentrations as the driving meteorological fields are degraded with coarser grid spacing
133 and also as different vertical levels within the model are used.

134 The guiding questions of this paper are, as follows:



- 135 1. How do atmospheric flows in mountainous areas affect CO₂ concentrations and their
136 representation in models?
137 2. What are the errors incurred due to the use of coarse-scale atmospheric simulations?
138 3. How can mountaintop CO₂ observations be used in an effective manner to constrain
139 regional carbon fluxes in complex terrain?

140 2. Methodology

141 2.1 RACCOON Observations

142 The Regional Atmospheric Continuous CO₂ Network (RACCOON,
143 <http://raccoon.ucar.edu>) was established in 2005 and has collected in situ CO₂
144 measurements at up to six sites over the past decade (Stephens et al., 2011). Here we
145 present and simulate observations from the three longest running high-alpine sites (Fig. 2;
146 Table 1). The easternmost site (NWR) is at 3,523 m elevation near the treeline on Niwot
147 Ridge, just west of Ward, CO. Niwot Ridge is a LTER site and there is an AmeriFlux
148 tower run by the University of Colorado 3 miles east and 500 m lower on the ridge. The
149 instrumentation reside in the “T-Van” where the U.S. National Oceanic and Atmospheric
150 Administration (NOAA)'s Global Monitoring Division has collected weekly flask
151 samples for measurement of CO₂, isotopes, and other species for over 40 years, and daily
152 flasks since 2006. The middle site (SPL) is at the Desert Research Institute's Storm Peak
153 Lab (3,210 m on Mt. Werner near Steamboat Springs, CO). This mountaintop
154 observatory has a long history of measurements related to cloud physics, cloud-aerosol
155 chemistry, and air quality. The westernmost site (HDP) is on Hidden Peak (3,351 m,
156 above the Snowbird ski resort, Utah). This mountaintop site generally experiences
157 regionally well-mixed or free-tropospheric air, but with influences from Salt Lake City
158 during boundary-layer growth and venting periods.

159 The RACCOON measurements are based on a LiCor LI-820 single-cell IRGA
160 with frequent calibrations. The instruments sample air from one of three inlet lines on a
161 tower (two at HDP) and use a suite of four calibration gases plus a fifth surveillance gas.
162 All reference gases are rigorously tied to the WMO CO₂ Calibration Scale with use of the
163 NCAR CO₂ and O₂ Calibration Facility. 100-second average measurement precision is ±
164 0.1 ppm (1 σ), and intercomparability is estimated from several methods to be 0.2 ppm
165 (Stephens et al., 2011).

166 We filtered out observations in which the within-hour standard deviation is
167 greater than 1.0 ppm or when the differences between the top two inlets are greater than
168 0.5 ppm, which indicate periods when significant influences that are highly localized to
169 the site are affecting the observations. This filtering removed 15%, 16%, and 27% of the
170 hourly observations at HDP, SPL, and NWR, respectively. Regardless, filtering made
171 negligible differences in the observed diurnal cycles in CO₂ (see Supplement).
172 Henceforth, we will refer to the filtered observations when discussing the observed CO₂.

173 2.2 WRF-STILT Atmospheric Model

174 The atmospheric modeling framework adopted in this study is a Lagrangian time-
175 reversed particle dispersion model, the Stochastic Time-Inverted Lagrangian Transport
176 (STILT) model (Lin et al., 2003), driven by a mesoscale gridded model, the Weather
177 Research and Forecasting (WRF) model (Skamarock and Klemp, 2008). STILT is a



178 Lagrangian model that simulates the effects of turbulent dispersion using the stochastic
179 motions of air parcels. It has been widely applied to the interpretation of CO₂ and trace
180 gases in general (Lin et al., 2004;Hurst et al., 2006;Göckede et al., 2010;Kim et al.,
181 2013;Mallia et al., 2015;Jeong et al., 2012). WRF is a state-of-the-art non-hydrostatic
182 mesoscale atmospheric model that can simulate a variety of meteorological phenomena
183 (Skamarock and Klemp, 2008), gaining widespread acceptance and usage among the
184 atmospheric science community. Careful coupling between WRF and STILT has been
185 carried out, with an emphasis towards physical consistency and mass conservation
186 (Nehrkorn et al., 2010).

187 For this study, we ran WRF in a nested mode centered between Utah and
188 Colorado where the RACCOON sites are located (Fig. 2). The grid spacing was refined
189 in factors of 3, from 12 km grid spacing covering the entire Western U.S. to 4 km and
190 then to 1.3 km in the innermost domain that covers all of the RACCOON sites. 41
191 vertical levels were adopted, with 10 of these levels within 1 km of the ground surface,
192 following Mallia et al. (2015). Comprehensive testing of different WRF settings—e.g.,
193 convection, microphysical, and planetary boundary layer (PBL) schemes—have been
194 carried out as part of a previous publication (Mallia et al., 2015), and we refer the reader
195 to that paper for details regarding the WRF configuration. In addition to the testing
196 reported in Mallia et al. (2015), we have also carried out evaluation of the WRF fields
197 specifically using meteorological measurements on mountaintops, near the RACCOON
198 sites. These evaluations reveal that errors in the simulated meteorological fields are
199 reasonable when compared against other atmospheric simulations evaluated in less
200 complex terrain (Mallia et al., 2015), and biases are especially small for the WRF-1.3km
201 fields (Table 2). In this paper, we will examine the resulting differences in
202 meteorological and CO₂ simulations when STILT is driven by WRF fields at three
203 different grid spacings.

204 In addition to the three WRF domains, we drove STILT with a fourth
205 meteorological field, from NCEP's Global Data Assimilation System (GDAS). GDAS is
206 archived at 1°×1° grid spacing, at 6 hourly intervals and at 23 vertical pressure levels.
207 Driving STILT with GDAS was a means by which we attempted to construct an
208 atmospheric model to resemble the NOAA CarbonTracker product, which was also at
209 1°×1° resolution (and 25 vertical levels) over North America. More details about
210 CarbonTracker can be found in the next section.

211 Driven by the various meteorological fields, STILT released 2000 air parcels
212 every 3 hours (00, 03, 06, ...21 UTC) for the months of June, July, and August 2012
213 from the RACCOON sites and transported for 3 days backward in time. An example of
214 STILT-simulated air parcel trajectories can be found in Fig. S1. The choice of 2000
215 parcels followed from results from sensitivity tests in a previous study, also over the
216 Western U.S. (Mallia et al., 2015). In the case of WRF, STILT has the capability to
217 transport the parcels in a nested fashion. So when we refer to “WRF 1.3km simulations”,
218 it actually means that the atmosphere in the innermost domain (Fig. 2) was simulated at
219 1.3 km, switching to 4km grid spacing when the parcel left the 1.3km domain; likewise,
220 the 12km winds were used when the parcel left the 4km domain. For the “WRF 4km
221 simulations” we started with the 4 km fields as the innermost domain, and then 12 km in
222 the outer domain.



223 For each site, we released STILT parcels using two different ways to determine
224 starting levels. When we refer to “AGL”, we mean that the starting height was set at the
225 level of the inlet above the ground surface (Table 1), following the local terrain as
226 resolved in the meteorological model (whether at 1.3-, 4-, 12-km, or 1° grid spacing).
227 The alternative method, referred to as “ASL”, means that the starting level was set to the
228 elevation above sea level. For instance, the HDP site is located at 3351 m above sea level.
229 The ground height as resolved by the 12km WRF model is at 2357 m, so the starting
230 height was placed at 994 (=3351 – 2357) m above the resolved terrain. CarbonTracker,
231 as well as many other global-scale models (Geels et al., 2007; Peters et al., 2010) places
232 the observation site at an internal model level following the ASL method, so the “GDAS-
233 ASL” runs were a means by which we attempted to mimic the global model configuration
234 and to illuminate potential errors that could result from such a configuration. We also
235 tested the AGL height for GDAS, at HDP only. As shown later, these runs were highly
236 erroneous, so we did not carry them out for the other two sites.

237 The STILT-simulated air parcels were tracked as they were transported
238 backwards in time from the RACCOON receptors (see example in Fig. S1); when they
239 were in the lower part of the PBL, the locations of the parcels and amount of time the
240 parcels spend in the lower PBL were tallied. This information was used in calculation of
241 the “footprint”—i.e., the sensitivity of the receptor to upwind source regions (in units of
242 concentration per unit flux). For more details, see Lin et al. (2003). The footprints,
243 encapsulating the atmospheric transport information, were then combined with gridded
244 fluxes from the biosphere and anthropogenic emissions, which are described in the next
245 sections.

246 **2.3 CarbonTracker CO₂ Concentrations and Biospheric Fluxes**

247 CarbonTracker is a carbon data assimilation system covering the whole globe that
248 retrieves both oceanic and terrestrial biospheric carbon fluxes (Peters et al., 2007).
249 Observed atmospheric CO₂ concentrations are assimilated by CarbonTracker, which
250 adjusts carbon fluxes to minimize differences with the observed CO₂ using an ensemble
251 Kalman filter methodology.

252 We took three-dimensional CO₂ fields from CarbonTracker to initialize CO₂
253 concentrations at the end of the 3-day back trajectories from STILT. CarbonTracker-
254 derived biospheric fluxes, along with anthropogenic and fire emissions (Sect. 2.4), were
255 also multiplied with STILT-derived footprints and combined with the initial CO₂
256 concentrations to yield simulated CO₂ at the RACCOON receptors.

257 CarbonTracker is maintained and continues to be developed by the NOAA's Earth
258 System Research Laboratory. For this paper, we adopt the “CT-2013b” version. CT-
259 2013b provides multiple prior estimates of the oceanic, terrestrial, and fossil carbon
260 fluxes, with each combination yielding separate posterior fields of carbon fluxes and CO₂
261 distributions. CT-2013b results are presented as an average across the suite of prior
262 fluxes and CO₂ fields.

263 CT-2013b resolves atmospheric transport and fluxes at 1°×1° over North America
264 and 3°-lon × 2°-lat in the rest of the globe, with 25 vertical levels. The driving
265 meteorological fields come from the European Centre for Medium-Range Weather
266 Forecasts' ERA-interim reanalysis. The ensemble Kalman filter system within
267 CarbonTracker solves for scaling factors on weekly timescales to adjust upward or
268 downward biospheric carbon fluxes. The adjustments were made over “ecoregions” on



269 land, rather than attempting to adjust fluxes within individual gridcells, as way to reduce
270 the dimensions of the inversion problem within CarbonTracker. More details regarding
271 the CarbonTracker system can be found in Peters et al. (2007) and on-line at
272 <http://www.esrl.noaa.gov/gmd/ccgg/carbontracker/CT2013B/>.

273 Since CarbonTracker was designed for global carbon cycle analyses to retrieve
274 large-scale fluxes, the adjustment to biospheric carbon fluxes could result in artifacts at
275 the local to regional scales. More specifically, the attempt to match CO₂ observations
276 with a single scalar can result in flipped diurnal cycles, causing carbon uptake during the
277 night that is partly offset by enhanced respiration in a nearby ecoregion (Fig. S2). For this
278 paper, we implemented a fix that removed this artifact, preserving the 24-hour integrated
279 carbon flux (Fig. S3).

280 2.4 Anthropogenic and Fire Emissions

281 Anthropogenic CO₂ emissions were obtained from the Emission Database for
282 Global Atmospheric Research (EDGAR) (European Commission, 2009), which resolves
283 emissions globally at 0.1°×0.1° annually. In order to temporally downscale the annual
284 emissions, hourly scaling factors were obtained from the Vulcan emission inventory
285 (Gurney et al., 2009) and applied to the EDGAR annual emissions. Lastly, CO₂ emissions
286 from EDGAR for Year 2010 were extrapolated to 2012 using population growth rates
287 across the U.S. since 2010, as this was the last year in which EDGAR emissions were
288 available.

289 Wildfire emissions for CO₂ were obtained from the Wildland Fire Emissions
290 Inventory (WFEI) (Urbanski et al., 2011). Since these emissions were only reported daily,
291 three-hourly diurnal scaling factors were obtained from Global Fire Emissions Database
292 v3.1 and applied to the daily WFEI emissions to downscale the emissions to sub-daily
293 timescales (Mu et al., 2011; van der Werf et al., 2010).

294 Contributions from anthropogenic and wildfire emissions, on average, to the mean
295 CO₂ diurnal cycle observed at all the mountain sites were secondary in comparison to the
296 biosphere (Fig. S4). In particular, the wildfire contributions were episodic and averaged
297 out to negligible contributions over Jun~Aug 2012. Because of this, we will not touch
298 upon wildfires in the remainder of the paper.

299 3. Results

300 3.1 Observed versus Simulated Diurnal Cycle

301 The observed and simulated diurnal cycles of CO₂ for the three selected RACCOON sites
302 are shown in Fig. 3. The observed diurnal cycle exhibits an amplitude of ~2 ppm, on
303 average, with more elevated concentrations at night and depleted values during the day.

304 In contrast to the observed diurnal cycles, the simulated CO₂ extracted from
305 CarbonTracker output exhibits a different cycle. Instead of peaking at night, CO₂ in
306 CarbonTracker reaches its maximum during the afternoon at HDP. At SPL and NWR,
307 the diurnal cycle is significantly attenuated, with nighttime values barely elevated over
308 the background instead of the nighttime enhancement in the observed values.

309 It appears that the erroneous diurnal pattern at HDP within CarbonTracker can
310 partly be due to the diurnal reversal in the original biospheric fluxes, which showed
311 strong uptake of CO₂ even at night for the gridcell where HDP is located (Fig. S2). This



312 resulted in erroneous diurnal patterns at all of the lowest 8 levels of CarbonTracker (Fig.
313 S5), with the bottom 2 levels exhibiting strong depletions in CO₂ at night and
314 enhancements during the day, pointing to unrealistic nighttime uptake and daytime
315 release.

316 However, the diurnal reversal in biospheric fluxes alone does not completely
317 explain the erroneous diurnal pattern. Differences in the diurnal pattern between GDAS-
318 ASL simulations after introducing the diurnal fix in biospheric fluxes were not as
319 pronounced at SPL and NWR.

320 The GDAS-ASL simulations show a pronounced peak of CO₂ in the morning that
321 is missing from observations at all three sites (Fig. 3). We will discuss this feature, also
322 seen in other coarse-scale simulations of mountaintop CO₂ (Geels et al., 2007), in Sect.
323 3.2 below.

324 In contrast to GDAS-ASL and CarbonTracker, the WRF-driven simulations better
325 reproduce the shape of the observed diurnal cycle (Fig. 3), with nighttime enhancements
326 and daytime depletions of CO₂. Considerable differences in nocturnal CO₂
327 concentrations are found, however, in the WRF-STILT runs at various grid spacings.
328 WRF-12km significantly overestimates CO₂ at night, while WRF-1.3km and -4km
329 produced similar CO₂ concentrations that correspond much more closely to observed
330 values. While GDAS simulations started near the ground (“GDAS-AGL”) also exhibit
331 nighttime enhancements and daytime depletions of CO₂, the nighttime values are grossly
332 estimated, exceeding even the values in WRF-12km. Therefore, we do not present
333 GDAS using the AGL configurations at the other two sites.

334 Part of the error in all the simulations against the observations could arise from
335 errors in the CarbonTracker boundary condition imposed at the end of the STILT back
336 trajectories. Evaluations of CT-2013b against aircraft vertical profiles (which were not
337 assimilated into CarbonTracker) at the Trinidad Head and Estevan Point sites on the West
338 Coast of the North American continent carried out by the CarbonTracker team
339 (<http://www.esrl.noaa.gov/gmd/ccgg/carbontracker/CT2013B/profiles.php>) indicate that
340 CT-2013b overestimates CO₂ concentrations by at most 1.0 ppm, on average, during the
341 summer season. Thus, the fact that GDAS and CarbonTracker underestimate CO₂ at
342 night likely cannot be attributed solely to a biased boundary condition.

343 3.2 Differences in Simulated Transport to Mountaintop Sites

344 3.2.1 Footprint Patterns

345 In order to isolate the impact of differences in atmospheric transport on the simulated
346 CO₂, we examine the average diurnal pattern of the footprint strength over Jun~Aug
347 2012 (Fig. 4). At each hour of the day we summed the spatially explicit map of the
348 average footprint that marks out the source region of each RACCOON site—shown in
349 Figs. 5–6 for HDP and in the Supplemental Information for the other 2 sites. The result
350 shows the diurnal pattern of the sensitivity of the receptor concentration to upwind fluxes.

351 To a large extent, the diurnal variation in footprint strength mirrors the simulated
352 CO₂ concentrations. Nocturnal enhancements in the footprints are seen in the WRF-
353 driven simulations, with the WRF-12km exhibiting the strongest nocturnal footprints.
354 Footprints from WRF-1.3km and WRF-4km are weaker at night than from WRF-12km
355 and closely resemble each other. GDAS-AGL footprints (only shown at HDP) are the
356 highest among all models at night, leading to the drastic overestimation in CO₂ in Fig. 3.



357 In contrast, GDAS-ASL footprints exhibit a peak in the morning and are generally
358 smaller in value than their WRF counterparts at other times of the day at HDP and NWR.
359 At SPL, the GDAS-ASL footprint strengths are stronger and more in line with values
360 from the other models.

361 Footprints are weaker during the daytime, and in contrast to the nighttime,
362 differences between footprint strengths simulated by different models are significantly
363 smaller. In particular, the differences are minimized in the afternoon.

364 These patterns are also seen in the footprint maps. We further examine
365 differences in the spatial patterns of average footprints produced from the various WRF
366 and GDAS configurations. The spatial patterns are contrasted at two different times of
367 the day, associated with the nighttime and afternoon hours: 0200MST (0900UTC) and
368 1400 MST (2100UTC), respectively. Only HDP is shown for these two hours of the day
369 in Figs. 5 and 6; similar figures for SPL and NWR can be found in the Supplementary
370 Information (Figs. S6~S9). The footprint maps show marked differences at night (Fig. 5):
371 the WRF-12km footprints are clearly stronger than their counterparts from the other 3
372 model configurations, with higher values covering the Wasatch Range near the HDP site.
373 Meanwhile, the GDAS-ASL footprint at 0200 MST shows a striking contrast, with very
374 low values around HDP and the Wasatch area in general.

375 The afternoon footprints at 1400MST (Fig. 6) display much more similarity with
376 each other. Not only do the spatial patterns between the WRF and GDAS runs resemble
377 one another; the significant differences in footprint strengths, with overestimation by
378 WRF-12km and underestimation by GDAS-ASL, are no longer found. The
379 aforementioned nighttime divergence and afternoon correspondence between footprint
380 patterns are repeated at the SPL and NWR sites (Figs S6~S9).

381 To further understand the nighttime divergence between model configurations, we
382 now examine the average air parcel trajectories within Figs 5 and 6. It is worth noting
383 that these trajectories differ from conventional mean wind trajectories that do not
384 incorporate effects from turbulent dispersion (Lin, 2012). Instead, these mean trajectories
385 are determined by averaging the 2000 stochastic air parcel trajectories from STILT used
386 for simulating transport arriving at a specific hour at a particular site, and then averaging
387 over the ~90 days spanning June~August 2012. Thus there are ~180,000 stochastic
388 trajectories averaged into generating the mean trajectory, thereby incorporating the net
389 effect of turbulence on atmospheric transport. An example showing a subset of stochastic
390 air parcels giving rise to the average trajectory is given in Fig. S1 for NWR, for 1400
391 MST.

392 Similar to the footprints, average trajectories differ much more at night than in the
393 afternoon. Differences in average air parcel trajectories and the underlying resolved
394 mountainous terrain are further examined in the next section.

395 3.2.2 Three-dimensional Terrain and Trajectories

396 The 3D terrain plots in Figs. 7, 9, and 11 illustrate the degradation in terrain
397 resolved by coarser grid spacings and the resulting differences in average STILT-derived
398 stochastic air parcel trajectories started at night (0900UTC) from the three sites. The
399 afternoon (2100UTC) plots are shown in the Supplementary Information (Figs. S10~S12).
400 The PBL heights, which determine whether air parcels are affected by surface fluxes (and
401 lead to nonzero footprint values) are also plotted as blue lines in the same plots. Note



402 that the apparent intersection of the PBL height with the ground in Figs. 7 and 9 is an
403 artifact from averaging of multiple PBL heights along stochastic trajectories (Fig. S1).

404 Despite terrain smoothing compared against WRF-1.3km, WRF-4km produced
405 STILT trajectories that are very similar to those from WRF-1.3km at all three sites,
406 suggesting that salient features of the mountain flows resolved with 1.3km spacing are
407 also found in the 4km spacing. In contrast, WRF-12km and GDAS-ASL both differed
408 significantly from the more finely-gridded WRF simulations. Not only did the
409 trajectories deviate from the higher resolution counterparts; the relationships between the
410 trajectory vis-à-vis the PBL height, critical for determining footprints and simulating CO₂
411 changes (Sect. 2.2), also differ. The WRF-12km trajectories spend more time within the
412 PBL, while GDAS-ASL trajectories are found much less within the PBL, because they
413 start at a greater height above ground level.

414 An alternative perspective is to view the trajectory and PBL heights relative to the
415 ground surface ("AGL") instead of above sea level, at each time step backward in time
416 from the receptor (Figs. 8, 10, 12). These figures highlight the fact that while PBL
417 dynamics in the three WRF configurations are similar, the heights of the trajectories
418 relative to the PBL height differ. The trajectory exits above the nocturnal PBL one hour
419 backward in time, on average, while the WRF-12km trajectory spends several hours
420 within the PBL.

421 The difference in the trajectory behavior can be explained by the differing terrain.
422 In mountainous terrain, PBL heights generally follow the terrain elevations, albeit with
423 attenuated amplitude (Steyn et al., 2013). Thus in WRF-1.3km and 4km, the more highly
424 resolved terrain produced shallow nocturnal PBL height that descend in the valley (Fig. 7)
425 while the corresponding trajectory hovers above it. Viewed relative to the ground surface
426 (Fig. 8), the trajectory originating from HDP appears to have exited above the nocturnal
427 PBL in WRF-1.3km and 4km. In contrast, due to the significantly "flattened" mountains
428 in WRF-12km and in GDAS, the PBL heights exhibit less spatial variation near the
429 mountaintop receptor, since the terrain itself was smoothed. Consequently, WRF-12km
430 trajectories, unlike the WRF-1.3km or -4km cases, travel closer to the ground surface,
431 within the nighttime PBL, even as it is advected away from the three RACCOON sites
432 (Figs. 7, 8). This resulted in stronger nighttime footprints in WRF-12km as seen in Figs.
433 4 and 5. Another effect of the proximity of the air parcels to the model's ground surface
434 is the slower windspeeds from surface drag, causing the air parcel trajectories to remain
435 close to the 3 sites until the previous day; for HDP and SPL, the mean trajectories spiral
436 toward the site at the surface, following an "Ekman wind spiral" pattern (Holton, 1992).
437 In WRF-1.3km or WRF-4km, the measurement sites are at significantly higher elevations
438 above the resolved valleys in the area surrounding the sites, and the air parcels are found
439 above the shallow nocturnal boundary layer hugging the valley floor, on average (Fig. 7).

440 Although both WRF-12km and GDAS poorly resolve the mountains, a key
441 difference in the case of GDAS-ASL is that the air parcels were released at a site's
442 elevation above sea level (following what is generally done in CarbonTracker, and other
443 global models), much higher above ground than the release used in WRF-12km, which
444 was selected to be the height in AGL above the flattened mountain. Therefore, the
445 GDAS-ASL trajectories were significantly higher than the PBL height in the model
446 (particularly at HDP and NWR), which followed the flattened ground surface in the $1^{\circ} \times 1^{\circ}$
447 grid spacing. Another noticeable difference in GDAS-ASL trajectory was the



448 significantly higher daytime PBL heights (Figs. 8, 10, 12). We suspect this is because of
449 the greatly reduced vertical resolution within GDAS (23 levels versus 41 levels in WRF):
450 since STILT diagnoses the PBL height to correspond to a model level, a higher PBL
451 height was chosen for GDAS because of the thicker vertical level. Another subtle artifact
452 of the coarse resolution within GDAS can be seen in the anomalously low daytime PBL
453 height just in the vicinity of HDP (Figs. 13, S10). It appears that the GDAS model set an
454 entire $1^{\circ} \times 1^{\circ}$ grid box near HDP to be water body (the Great Salt Lake), thereby
455 suppressing the PBL height.

456 The three-dimensional plots can explain the higher nighttime footprint strengths at
457 SPL (Figs. 4, S6). This result appears to be a consequence of the relative elevation of the
458 site and surrounding terrain. The elevation of the surrounding valley floor at SPL is
459 closer to that of the mountaintop location of SPL (Fig. 9); therefore, air parcels released
460 from SPL would have a stronger tendency to reside within the PBL even over the
461 surrounding valleys, unlike the steeper dropoff--i.e., deeper valley--upwind of HDP (Fig.
462 7) and NWR (Fig. 11).

463 As already found in the footprints (Fig. 5), the afternoon (2100 UTC) differences
464 in air parcel trajectories are much smaller (Figs. S10~S12). We suspect that this is due to
465 the fact that the deeper daytime PBL height causes the trajectories to reside within the
466 PBL, and stronger mixing within the daytime PBL minimize the relative terrain
467 differences. A previous modeling study focusing on the SPL area has also suggested the
468 daytime afternoon PBL depth to extend above the mountaintop (De Wekker et al., 2009),
469 indicating that differences between terrain resolution and the resulting flows could be
470 reduced due to the strong mixing taking place within the deep afternoon PBL.
471 Consequently, simulations in the afternoon show much smaller divergence between
472 various model configurations, resulting in similar footprint strengths and CO₂ values
473 (Figs. 3 and 4). More evidence of the convergence in afternoon simulated CO₂ can be
474 found in the small differences in CO₂ modeled at CarbonTracker's different levels during
475 this time (Fig. S5).

476 A few studies have specifically focused on the flows and atmospheric transport
477 around the NWR site. These authors have pointed to thermally driven flows, particularly
478 downslope drainage flow events at night (Sun et al., 2007; Sun and De Wekker,
479 2011; Blanken et al., 2009). Daytime upslope events, while weaker, were also noted (Sun
480 and De Wekker, 2011; Blanken et al., 2009; Parrish et al., 1990). It may seem that the 3D
481 trajectories in Fig. 11 and Fig. S12 run counter to the presence of such thermally driven
482 flows. We suspect that this is because the thermally driven flows induced by the terrain
483 cannot be discerned in the mean trajectories, which also reflect the larger scale flows that
484 can be stronger than the local scale thermally driven flows (Zardi and Whiteman, 2013).
485 When one examines the stochastic trajectories from which the mean trajectories are based
486 (Fig. S1), it is clear that some upslope trajectories can be detected.

487 We now examine the reason for the erroneous daytime peak in simulated CO₂
488 from GDAS-ASL that does not show up in the observations (Fig. 3). We specifically
489 focus on this feature because the daytime peak was also found in other coarse-scale
490 simulations of CO₂ for mountaintop sites--e.g., in Europe (Geels et al., 2007). Focusing
491 on the three-dimensional plots at the hours of 0800 and 1100 MST (Fig. 13), when the
492 simulated peaks are found at SPL and both NWR/HDP, respectively, the peaks coincide
493 with times when average trajectories are found within a relatively shallow morning PBL.



494 As the air parcels move backward in time, when the morning transitions backward in
495 time to the nighttime, many of them would still be found within the shallow nighttime
496 PBL. Due to the shallowness of the nocturnal PBL, the footprint values for the air
497 parcels found there would be high. These parcels would also be sampling the nighttime
498 CO₂ release and therefore lead to enhancements in CO₂. In other words, the erroneous
499 daytime peak reflects enhanced CO₂ that is vented up to the observing height within the
500 model during the day. We suspect that something similar is taking place in other global
501 models, leading to similar erroneous daytime CO₂ peaks (Geels et al., 2007).

502 **4. Discussion**

503 This study has sought to answer the question: how can mountaintop CO₂ observations be
504 used to constrain regional scale carbon fluxes, given the complex terrain and flows in the
505 vicinity of mountaintop sites? To address this question, we have driven a Lagrangian
506 particle dispersion model simulating the transport of turbulent air parcels arriving at 3
507 mountaintop CO₂ sites in the Western U.S. We then examined potential differences in
508 simulated results as the atmospheric simulations are driven by meteorological fields
509 resolved with differing grid spacings and at different vertical levels.

510 We found that the observed average diurnal CO₂ pattern is better reproduced by
511 simulations driven by WRF-1.3km and WRF-4km ("AGL" configuration), with minimal
512 differences between the two configurations (Fig. 3). The coarser-scale models (WRF-
513 12km_AGL, GDAS-1°, and CarbonTracker) fail to reproduce the observed diurnal
514 pattern at all 3 sites. The problem is especially severe at night, when both GDAS-ASL
515 and CarbonTracker lack the nocturnal enhancements. In contrast, WRF-12km (AGL)
516 shows nocturnal CO₂ buildup that is clearly too strong. The overestimation problem is
517 exacerbated when both coarser grid spacing and "AGL" configuration are adopted, as
518 seen in GDAS-AGL at HDP (Fig. 3).

519 The overestimate in nighttime CO₂ from WRF-12km (AGL) is due to the
520 preponderance of simulated air parcels found within the nocturnal PBL (Figs. 7~9),
521 which can be traced to the fact that air parcels are closer to the ground surface when
522 mountains are flattened. Conversely, when released at "ASL" levels air parcels are found
523 much higher above the nocturnal PBL due to the flattening of mountains in a coarse-scale
524 global model like GDAS, resulting in minimal sensitivity to nighttime biospheric fluxes
525 and lack of CO₂ buildup. Such large errors in estimated carbon fluxes due to lack of
526 ability to resolve patterns have also been found in earlier studies in Europe (Pillai et al.,
527 2011; Peters et al., 2010).

528 The natural question, then, is what can researchers do with mountaintop CO₂
529 observations, given the difficulty in resolving the terrain and flows in complex terrain?

530 **4.1 Approach 1: Adjust vertical level of simulations from which to compare against** 531 **observed values**

532 The diurnal cycle simulated within CarbonTracker varies significantly as a function of
533 the vertical level (Fig. S5) from which CO₂ is extracted, particularly at night. The
534 strongly attenuated diurnal cycle in the interpolated level corresponding to the ASL
535 elevation of the mountaintop sites (orange dashed) is found at higher levels within
536 CarbonTracker too, away from the first few levels near the ground. At HDP, the



537 nighttime depletion of CO₂ at lower levels appears to be due to the erroneous nighttime
538 photosynthetic uptake in the gridcell where HDP is located (Fig. S2).

539 Interestingly, at SPL and NWR the diurnal pattern at a level between Levels 2 and 3
540 appears to correspond more closely to the overall observed CO₂ diurnal cycle, perhaps
541 due to the presence of nighttime enhancements closer to the model surface that is absent
542 from the higher levels closer to the ASL elevation. The closer correspondence to
543 observed patterns may call for researchers to adjust the vertical level to maximize
544 resemblance to observations. This was carried out at Jungfraujoch (Folini et al., 2008),
545 where the authors simulated carbon monoxide (CO) at multiple heights and arrived at a
546 height of 80 m above the model's ground surface as the best correspondence with the
547 observed CO, which was measured closer to the ground (Rinsland et al., 2000). Instead,
548 a different study simulating observations at the same site adopted a height of 830 m
549 above the model ground surface (Tuzson et al., 2011). This example illustrates the
550 divergence in researchers' choices for the vertical level in the midst of mountainous
551 terrain.

552 It is worth noting that the introduction of additional degrees of freedom in the vertical
553 level in "fitting" the measured CO₂ diurnal cycle within a carbon assimilation system is
554 potentially problematic. The reason is that the assimilation system seeks to solve for
555 carbon fluxes by examining the mismatch between observed versus simulated CO₂
556 concentrations. If the mismatch is due to erroneous fluxes, the introduction of additional
557 degrees of freedom in the vertical level would compensate for erroneous fluxes. For
558 instance, if the nighttime carbon fluxes are overestimated in the model, this should show
559 up as an enhanced CO₂ concentration that is larger than observed values. However, this
560 overestimation in CO₂ would be reduced by picking a higher vertical level rather than
561 fixing the overly large efflux in the model. The optimal level could differ between night
562 and day as well; for instance, a level higher than Level 2 would fit better against
563 observations during the daytime at SPL and NWR (Fig. S5). If different levels are
564 adopted at different times of the day, the degrees of freedom that can be adjusted would
565 be even larger, and model-data mismatches would be used in vertical level adjustments
566 instead of correcting erroneous biospheric fluxes.

567 Regardless, there is some role for vertical level adjustments to remove the gross
568 mismatch in the observed vs simulated diurnal cycles. If the vertical level is indeed
569 adjusted in a carbon inversion system, we suggest that additional information (e.g.,
570 comparisons to meteorological observations or other tracers) is used rather than
571 maximizing the match to the target species (i.e., CO₂, in the case of a carbon inversion
572 system).

573 The CO₂ values at multiple levels within CarbonTracker show that unlike the
574 nighttime, differences between vertical levels are much smaller during the afternoon at
575 SPL and NWR (Fig. S5), suggesting that the simulated CO₂ values are not as sensitive to
576 the choice of vertical level. We suspect that the large differences between vertical levels
577 at HDP is due to the flipped diurnal cycle in biospheric fluxes within CarbonTracker (Fig.
578 S3). Otherwise, the lack of sensitivity to the choice of vertical level suggests that coarse-
579 scale models should assimilate afternoon observations, rather than nighttime observations
580 (see "Approach 4" below).



581 **4.2 Approach 2: Reject mountaintop data**

582 Due to the dangers of mis-representing terrain/flows and introducing biases into the
583 carbon inversion system, an obvious way to deal with this problem is to neglect the
584 mountaintop data altogether. This is already commonly practiced within carbon
585 inversion systems (Rodenbeck, 2005;Geels et al., 2007;Peters et al., 2010). In fact, the
586 most recent release of CarbonTracker (“CT-2015”) stopped assimilating the three
587 RACCOON sites (<http://www.esrl.noaa.gov/gmd/ccgg/carbontracker/>).

588 However, the absence of mountaintop CO₂ observations to constrain carbon
589 inversion systems is, in effect, throwing away valuable information that could inform
590 carbon exchange in potentially important areas of the world (Fig. 1). Case in point is the
591 Schauinsland CO₂ time series on a mountain in the middle of Western Europe, which as
592 of this writing has collected over 40 years of continuous CO₂ data (Schmidt et al., 2003)
593 but remains excluded from numerous carbon inversion systems (Rodenbeck, 2005;Geels
594 et al., 2007;Peters et al., 2010).

595 **4.3 Approach 3: Assign errors to account for model errors**

596 Instead of neglecting the mountaintop CO₂ observations altogether, an alternative
597 approach is to make use of the observations, but assigning them errors within the model-
598 measurement discrepancy error covariance matrix to account for model deficiencies (Lin
599 and Gerbig, 2005;Gerbig et al., 2008). In this way, the inversion system would assign
600 less weight to observations that the model has difficulties simulating. Given the
601 systematic misrepresentation of the diurnal cycle in coarse-scale models, particularly at
602 night (Fig. 3), this approach will effectively throw away much of the data as noise, due to
603 inadequacies in the model. This naturally leads to the next possible approach of just
604 having coarse-scale models assimilate afternoon observations.

605 **4.4 Approach 4: Have coarse-scale models assimilate afternoon observations
606 instead of nighttime**

607 Our results show that the simulated CO₂ values are more in accordance with observed
608 values in the afternoon (Fig. 3). This follows from the fact that afternoon trajectories and
609 footprints match their higher resolution counterparts (Figs. 6, S7, S9, S10~S12), likely
610 due to the deeper afternoon PBL depth and the reduction of terrain effects (Steyn et al.,
611 2013). In other words, relative differences in PBL depth associated with flattening of
612 mountains are lessened when the PBL is deeper; thus the impact on whether an air parcel
613 sampled by the mountaintop site falls within the PBL is also attenuated under afternoon
614 vigorous mixing conditions.

615 Based on these results, and in lieu of better transport, we suggest coarse-scale
616 models may be better served to assimilate afternoon observations over the continent at
617 their above sea level elevation. This is contrary to what has been commonly practiced by
618 researchers, when nighttime mountaintop observations were assimilated (Peters et al.,
619 2007;Keeling et al., 1976) to avoid daytime upslope flows and when nocturnal
620 observations that represent free tropospheric conditions would better match coarse
621 resolution models. We have found that sampling coarse-scale (1 deg) models at the
622 corresponding ASL height have significant difficulties simulating nighttime CO₂, since it
623 appears that the model failed to represent the strength of the nocturnal footprint at the 3
624 RACCOON mountaintop sites (Figs. 4, 5). Thus the inability of coarse-scale models to
625 simulate the transport and PBL depths result in the lack of nocturnal enhancements and



626 thereby the wrong diurnal cycle (Fig. 3). Conversely, sampling the 12-km simulation at
627 the AGL height also has significant difficulties simulating nighttime CO₂, because it
628 overestimates the nocturnal footprint.

629 However, careful attention needs to be paid to upslope flows in the afternoon and
630 the potential mis-interpretation of more localized biospheric signals or anthropogenic
631 signals from below the mountain. A study from Jungfraujoch in Europe suggested that as
632 much as ~40% of the days in a year are influenced by thermally driven flows (Griffiths et
633 al., 2014). During the afternoon, the mountaintop site would then be influenced by
634 thermally driven upslope winds, as also pointed out by a number of studies around NWR,
635 along the Colorado Front Range (Sun et al., 2010; Sun and De Wekker, 2011; Parrish et al.,
636 1990) as well as SPL (De Wekker et al., 2009). For sites like HDP and NWR, which
637 have large nearby urban areas at lower elevation, upslope conditions can be of particular
638 concern if not properly accounted for. If these sites experience elevated CO₂ in the
639 afternoon from pollution sources, and this transport is not captured by the models, then
640 natural CO₂ sources can be significantly overestimated.

641 We found it encouraging that despite the proximity of significant population and
642 anthropogenic emissions from the Salt Lake and Denver area to the HDP and NWR sites,
643 respectively, the WRF-1.3km model suggests that the additional contribution of
644 anthropogenic CO₂ in the afternoon, over and beyond the nighttime signal is less than
645 1ppm, on average (Fig. S4). Presumably this is because of the high elevation of HDP and
646 NWR in relation to the urban area and the dilution of signals as they move up slope; the
647 afternoon urban signal would be enhanced if the sites were placed at lower peaks.

648 Regardless, it is prudent to consider mountaintop sites as not necessarily “pristine”
649 sites and to consider potential contributions from surrounding anthropogenic emissions
650 on these observations. It has been estimated that as of the year 2000, over 10% of the
651 world population live in mountainous areas (Huddleston et al., 2003), meaning that any
652 mountaintop site could very well see anthropogenic signatures. We recommend
653 additional tracers to be measured in conjunction with the mountaintop CO₂ sites. For
654 instance, combustion tracers such as C¹⁴ and CO (Levin and Karstens, 2007) have been
655 measured alongside CO₂ at mountaintop sites in Europe. Another promising tracer is
656 Rn²²² (Griffiths et al., 2014), which provides a measure of surface exchange and would
657 help provide constraints on the exchange of air measured at the mountaintop with the
658 surface. Co-located meteorological observations—whether in-situ or remotely-sensed
659 (e.g., radar, sodar, lidar)—to probe atmospheric flows and turbulent mixing would also
660 be of significant value in helping to interpret the tracer observations (Rotach et al.,
661 2014; Banta et al., 2013).

662 **4.5 Approach 5: Adopt high-resolution modeling frameworks**

663 The least problematic, though potentially costly in terms of computational time, approach
664 to reduce modeling errors when interpreting mountaintop CO₂ observations is to adopt a
665 high resolution modeling framework. This conclusion was also arrived at by previous
666 studies (Pillai et al., 2011; van der Molen and Dolman, 2007; De Wekker et al., 2009).
667 From our results, it appears that meteorological fields from WRF at 4-km grid spacing,
668 driving a Lagrangian particle dispersion model, can reproduce most features from a 1.3-
669 km simulation, and generate a CO₂ diurnal cycle that qualitatively matches the observed
670 pattern. Once the WRF fields are degraded to 12-km grid spacing, the model fails to
671 capture such features.



672 While at least 4-km resolution in the meteorological fields is needed for the sites
673 examined here in the American Rockies, we anticipate that the minimum resolution
674 would depend on the level of complexity in the terrain, the height of the observational
675 site, and relationship with surrounding sources/sinks.

676 5. Conclusions

677 Given the large extent of the Earth's surface covered by hills and mountains and the large
678 amount of biomass and potential for carbon storage in complex terrain (Fig. 1), we call
679 for expanded efforts in observing and modeling CO₂ and other tracers on mountaintop
680 sites. This study has illustrated the potential for even coarse-scale models to extract
681 information from these observations when focusing on the daytime, afternoon values, and
682 the ability of high resolution models to simulate the general features of the summertime
683 diurnal CO₂ cycle even in the midst of significant terrain complexity. However, we
684 acknowledge that even the highest resolution model adopted in this paper undoubtedly is
685 subject to limitations of its own, and that deviations between simulated versus observed
686 CO₂ diurnal cycles arise from errors in both atmospheric transport as well as the
687 biospheric fluxes. Due to the focus on atmospheric transport in this paper, errors in the
688 simulations caused by shortcomings in the biospheric fluxes remain outside the scope of
689 this study (except for corrections to the flipped diurnal cycle; Fig. S3)

690 Even though current models remain imperfect, we call for sustained and expanded
691 observations of CO₂ and other tracers (e.g., CO, ²²²Rn, and the isotopes of CO₂) co-
692 located with meteorological observations on mountaintop sites to create enhanced
693 datasets that can be further utilized by modeling frameworks of the future. Finally, we
694 call for testing and gathering of three-dimensional CO₂ observations over complex terrain,
695 as revealed by intensive airborne campaigns like the Airborne Carbon in the Mountains
696 Experiment (Sun et al., 2010).

697
698

699 Acknowledgements

700 This study was supported by NOAA Climate Program Office's AC4 program, award #
701 NA13OAR4310087 (UU). The RACCOON network has been supported by NSF (EAR-
702 0321918), NOAA (NA09OAR4310064) and DOE (DE-SC0010624 and DE-SC0010625).
703 The National Center for Atmospheric Research is sponsored by the National Science
704 Foundation. We thank site collaborators at the RACCOON sites: Ian and Gannet Hallar
705 at SPL, Dean Cardinale at HDP, and the CU Mountain Research Station and staff at
706 NWR. We thank J. Knowles for the meteorological data at NWR and S. Urbanski for
707 sharing the WFEI fire emission inventory. A. Andrews and A. Jacobson are gratefully
708 acknowledged for helpful discussions.

709
710
711



712 **Figure Captions**

713 **Fig. 1**

714 Aboveground biomass [mega-tons of carbon] from the North American Carbon Program
715 baseline dataset for year 2000 (Kellndorfer et al., 2013) overlaid on topographic surface
716 in the Western U.S., resolved at $0.5^{\circ} \times 0.5^{\circ}$ grid spacing.

717 **Fig. 2**

718 The WRF simulation domain, covering the Western U.S. with a series of nests with 12-,
719 4-, and 1.3-km grid spacing. These WRF meteorological fields are used to drive air
720 parcel trajectories within the STILT model.

721 **Fig. 3**

722 The average diurnal CO_2 pattern during June~August 2012 as observed at the 3
723 mountaintop sites in the RACCOON network: Hidden Peak (HDP), Storm Peak
724 Laboratory (SPL), and Niwot Ridge (NWR). Compared against the observations are
725 simulated diurnal CO_2 patterns from different models: CarbonTracker, STILT driven
726 with WRF at different grid spacings, and STILT driven with GDAS. Multiple GDAS-
727 driven STILT model configurations are shown, including runs without fixes to the
728 biospheric fluxes (“biofluxorig”; see Supplemental Information), as well as releasing air
729 parcels at the elevations of the sites above mean seal level (“ASL”) or, for HDP only, at
730 the inlet height (Table 1) above the model’s ground level (“AGL”). All of the WRF-
731 driven STILT runs place the release point of air parcels following the AGL configuration.

732 **Fig. 4**

733 The average diurnal footprint strengths at HDP, SPL, and NWR over June~August 2012
734 from STILT, driven with different meteorological fields and release heights (ASL vs
735 AGL). The footprint strength was derived by summing over the spatial distribution of
736 footprint values (Fig. 5).

737 **Fig. 5**

738 The average footprint (shown in \log_{10}) for the Hidden Peak (HDP) site in Utah, at night:
739 0200 MST (0900 UTC), gridded at $0.1^{\circ} \times 0.1^{\circ}$. The site is denoted as a triangle. The
740 average back trajectory (averaged over the stochastic STILT trajectories) is drawn as a
741 line, with points indicating trajectory locations every hour, as the trajectory moves back
742 from the site indicated as points. Red parts of the trajectory refer to the nighttime
743 (1900~0700 MST), while pink portions indicate the daytime (0700~1900 MST). Parts of
744 the trajectory are shaded with blue when it is found below the average height of the PBL
745 along the trajectory.

746 **Fig. 6**

747 Similar to Fig. 5, but for the afternoon: 1400 MST (2100 UTC) at HDP.

748 **Fig. 7**

749 Three dimensional plots of the terrain over a domain of $\sim 1^{\circ} \times 1^{\circ}$ surrounding HDP, as
750 resolved by the WRF and GDAS models at various grid spacings. The HDP site is
751 denoted as a triangle. Also shown is the average back trajectory, derived by averaging
752 locations of the numerous stochastic trajectories simulated by STILT, driven by the



753 various WRF meteorological fields and the global GDAS field. Back trajectories were
754 started from HDP at 0200 MST (0900 UTC). Points indicate trajectory locations every
755 hour, as the trajectory moves back from the site indicated as points. Red portions of the
756 trajectory refer to the nighttime (1900~0700 MST), while pink portions indicate the
757 daytime (0700~1900 MST). In addition, the PBL heights averaged along the
758 backtrajectory are shown as the blue line.

759 **Fig. 8**

760 Time series of the average back trajectory and PBL heights relative to the ground surface
761 ("AGL") instead of above sea level, at each time step backward in time from the receptor
762 (triangle). Red portions of the trajectory refer to the nighttime (1900~0700 MST), while
763 pink portions indicate the daytime (0700~1900 MST). The PBL heights averaged along
764 the backtrajectory are shown as the blue line. The nighttime PBL height is indicated in
765 dark blue, while the daytime portion is in light blue.

766 **Fig. 9**

767 Similar to Fig. 7, but for the Storm Peak Laboratory (SPL) site.

768 **Fig. 10**

769 Similar to Fig. 8, but for the Storm Peak Laboratory (SPL) site.

770 **Fig. 11**

771 Similar to Fig. 9, but for the Niwot Ridge (NWR) site.

772 **Fig. 12**

773 Similar to Fig. 10, but for the Niwot Ridge (NWR) site.

774 **Fig. 13**

775 Similar to three-dimensional terrain and trajectory plots as shown in Figs. 7, 9, and 11,
776 but for just the GDAS 1 deg. ASL simulations and for the morning hours of 0800 MST
777 and 1100 MST.

778



779 **Tables**
780

	Hidden Peak (HDP)	Storm Peak Lab (SPL)	Niwot Ridge (NWR)
Latitude/Longitude	40° 33' 38.80" N 111° 38' 43.48" W	40° 27' 00" N 106° 43' 48" W	40° 03' 11" N 105° 35' 11" W
Top Inlet Height	17.7 m	9.1 m	5.1 m
Site Altitude [m above sea level]	3351 m	3210 m	3523 m
Model Altitude:			
<i>WRF-1.3km</i>	2996 m	3038 m	3411 m
<i>WRF-4km</i>	2918 m	2818 m	3382 m
<i>WRF-12km</i>	2357 m	2724 m	3076 m
<i>GDAS</i>	1856 m	2757 m	2333 m
<i>CarbonTracker</i>	2004 m	2582 m	2276 m

781 **Table 1.** Characteristics of RACCOON mountaintop sites examined in this paper, as
782 well as the representation of terrain in different meteorological files at these sites.
783
784



785

Site	SPL				NWR			
	1.3-km WRF	4-km WRF	12-km WRF	GDAS	1.3-km WRF	4-km WRF	12-km WRF	GDAS
u-wind BIAS [m/s]	-0.5	-1.5	-0.9	2.3	0.1	-0.3	-1.4	-0.2
v-wind BIAS [m/s]	-0.6	-0.3	-0.2	1	0.2	0.4	0.9	1.1
u-wind RMSE [m/s]	3.1	3.8	3.2	3.7	3.5	3.4	3.4	3.2
v-wind RMSE [m/s]	2.7	2.7	2.3	2.5	2.2	2.1	2.2	3

786

787 **Table 2.** Comparisons of different meteorological files driving STILT against hourly-
788 averaged wind observations at Storm Peak Laboratory (-106.74 W; 40.45 N) and at
789 Niwot Ridge (-105.586 W; 40.053 N; 3502 m ASL) (Knowles, 2015), near the
790 RACCOON CO₂ site. Meteorological observations were not available at the Hidden Peak
791 site. Error statistics are presented separately for the west-to-east component ("u-wind")
792 and south-to-north component ("v-wind") of the wind velocity vector.

793

794 **References**

- 795 Anderegg, W. R. L., Berry, J. A., Smith, D. D., Sperry, J. S., Anderegg, L. D. L., and
796 Field, C. B.: The roles of hydraulic and carbon stress in a widespread climate-
797 induced forest die-off, *Proceedings of the National Academy of Sciences*, 109, 233-
798 237, 10.1073/pnas.1107891109, 2012.
- 799 Arora, V. K., Boer, G. J., Friedlingstein, P., Eby, M., Jones, C. D., Christian, J. R., Bonan,
800 G., Bopp, L., Brovkin, V., Cadule, P., Hajima, T., Ilyina, T., Lindsay, K., Tjiputra,
801 J. F., and Wu, T.: Carbon–Concentration and Carbon–Climate Feedbacks in CMIP5
802 Earth System Models, *Journal of Climate*, 26, 5289-5314, 10.1175/jcli-d-12-
803 00494.1, 2013.
- 804 Bakwin, P. S., Tans, P. P., Hurst, D. F., and Zhao, C.: Measurements of carbon dioxide
805 on very tall towers: results of the NOAA/CMDL program, *Tellus*, 50B, 401-415,
806 1998.
- 807 Baldocchi, D., Falge, E., Gu, L., Olson, R., Hollinger, D., Running, S., Anthoni, P.,
808 Bernhofer, C., Davis, K., Evans, R., Fuentes, J., Goldstein, A., Katul, G., Law, B.,
809 Lee, X., Malhi, Y., Meyers, T., Munger, W., Oechel, W., Paw U, K. T., Pilegaard,
810 K., Schmid, H. P., Valentini, R., Verma, S., Vesala, T., Wilson, K., and Wofsy, S.:
811 FLUXNET: A new tool to study the temporal and spatial variability of ecosystem-
812 scale carbon dioxide, water vapor and energy flux densities, *Bulletin of the*
813 *American Meteorological Society*, 82, 2415-2435, 2001.
- 814 Banta, R. M., Shun, C. M., Law, D. C., Brown, W., Reinking, R. F., Hardesty, R. M.,
815 Senff, C. J., Brewer, W. A., Post, M. J., and Darby, L. S.: Observational
816 Techniques: Sampling the Mountain Atmosphere, in: *Mountain Weather Research*
817 *and Forecasting: Recent Progress and Current Challenges*, edited by: Chow, K. F.,
818 De Wekker, F. J. S., and Snyder, J. B., Springer Netherlands, Dordrecht, 409-530,
819 2013.
- 820 Blanken, P. D., Williams, M. W., Burns, S. P., Monson, R. K., Knowles, J., Chowanski,
821 K., and Ackerman, T.: A comparison of water and carbon dioxide exchange at a
822 windy alpine tundra and subalpine forest site near Niwot Ridge, Colorado,
823 *Biogeochemistry*, DOI:10.1007/s10533-10009-19325-10539, 2009.
- 824 Brooks, B. G. J., Desai, A. R., Stephens, B. B., Michalak, A. M., and Zscheischler, J.:
825 Feasibility for detection of ecosystem response to disturbance by atmospheric
826 carbon dioxide, *Biogeosciences Discuss.*, 2016, 1-29, 10.5194/bg-2016-223, 2016.
- 827 Cox, P. M., Betts, R. A., Jones, C. D., Spall, S. A., and Totterdell, I. J.: Acceleration of
828 global warming due to carbon-cycle feedbacks in a coupled climate model, *Nature*,
829 408, 184-187, 2000.
- 830 De Wekker, S. F. J., Ameen, A., Song, G., Stephens, B. B., Hallar, A. G., and McCubbin,
831 I. B.: A Preliminary Investigation of Boundary Layer Effects on Daytime
832 Atmospheric CO₂ Concentrations at a Mountaintop Location in the Rocky
833 Mountains, *Acta Geophysica*, 57, 904-922, 2009.
- 834 Denning, A. S., Randall, D. A., Collatz, G. J., and Sellers, P. J.: Simulations of terrestrial
835 carbon metabolism and atmospheric CO₂ in a general circulation model. Part 2:
836 Simulated CO₂ concentrations, *Tellus*, 48B, 543-567, 1996.
- 837 Desai, A. R., Moore, D. J. P., Ahue, W. K. M., Wilkes, P. T. V., De Wekker, S. F. J.,
838 Brooks, B.-G., Campos, T., Stephens, B. B., Monson, R. K., Burns, S. P., Quaife,
839 T., Aulenbach, S. M., and Schimel, D. S.: Seasonal pattern of regional carbon



- 840 balance in the central Rocky Mountains from surface and airborne measurements,
841 Journal of Geophysical Research, 116, doi:10.1029/2011JG001655, 2011.
- 842 European Commission: Joint Research Centre/Netherlands Environmental Assessment
843 Agency, Emission Database for Global Atmospheric Research (EDGAR), in,
844 release version 4.0 ed., 2009.
- 845 Fisher, J. B., Sikka, M., Oechel, W. C., Huntzinger, D. N., Melton, J. R., Koven, C. D.,
846 Ahlström, A., Arain, M. A., Baker, I., Chen, J. M., Ciais, P., Davidson, C., Dietze,
847 M., El-Masri, B., Hayes, D., Huntingford, C., Jain, A. K., Levy, P. E., Lomas, M.
848 R., Poulter, B., Price, D., Sahoo, A. K., Schaefer, K., Tian, H., Tomelleri, E.,
849 Verbeeck, H., Viogy, N., Wania, R., Zeng, N., and Miller, C. E.: Carbon cycle
850 uncertainty in the Alaskan Arctic, Biogeosciences, 11, 4271-4288, 10.5194/bg-11-
851 4271-2014, 2014.
- 852 Folini, D., Uhl, S., and Kaufmann, P.: Lagrangian particle dispersion modeling for the
853 high Alpine site Jungfraujoch, Journal of Geophysical Research: Atmospheres, 113,
854 n/a-n/a, 10.1029/2007JD009558, 2008.
- 855 Friedlingstein, P., Dufresne, J. L., Cox, P. M., and Rayner, P.: How positive is the
856 feedback between climate change and the carbon cycle?, Tellus, 55B, 692-700,
857 2003.
- 858 Geels, C., Gloor, M., Ciais, P., Bousquet, P., Peylin, P., Vermeulen, A. T., Dargaville, R.,
859 Aalto, T., Brandt, J., Christensen, J. H., Frohn, L. M., Haszpra, L., Karstens, U.,
860 Rödenbeck, C., Ramonet, M., Carboni, G., and Santaguida, R.: Comparing
861 atmospheric transport models for future regional inversions over Europe –
862 Part 1: mapping the atmospheric CO₂ signals, Atmos. Chem. Phys., 7, 3461-3479,
863 10.5194/acp-7-3461-2007, 2007.
- 864 Gerbig, C., Korner, S., and Lin, J. C.: Vertical mixing in atmospheric tracer transport
865 models: error characterization and propagation, Atmospheric Chemistry and
866 Physics, 8, 591-602, 2008.
- 867 Gerbig, C., Dolman, A. J., and Heimann, M.: On observational and modelling strategies
868 targeted at regional carbon exchange over continents, Biogeosciences, 6, 1949-1959,
869 2009.
- 870 Göckede, M., Michalak, A. M., Vickers, D., Turner, D. P., and Law, B. E.: Atmospheric
871 inverse modeling to constrain regional - scale CO₂ budgets at high spatial and
872 temporal resolution, Journal of Geophysical Research, 115,
873 doi:10.1029/2009JD012257, 2010.
- 874 Gollehon, N., and Quinby, W.: Irrigation in the American West: Area, Water and
875 Economic Activity, International Journal of Water Resources Development, 16,
876 187-195, 10.1080/07900620050003107, 2000.
- 877 Griffiths, A. D., Conen, F., Weingartner, E., Zimmermann, L., Chambers, S. D., Williams,
878 A. G., and Steinbacher, M.: Surface-to-mountaintop transport characterised by
879 radon observations at the Jungfraujoch, Atmos. Chem. Phys., 14, 12763-12779,
880 10.5194/acp-14-12763-2014, 2014.
- 881 Gurney, K. R., Mendoza, D. L., Zhou, Y., Fischer, M. L., Miller, C. C., Geethakuma, S.,
882 and de la Rue du Can, S.: High resolution fossil fuel combustion CO₂ emission
883 fluxes for the United States, Environmental Science and Technology, 43, 5535-
884 5541, 2009.



- 885 Holton, J. R.: An introduction to dynamic meteorology, Academic Press, San Diego,
886 1992.
- 887 Huddleston, B., Ataman, E., de Salvo, P., Zanetti, M., Bloise, M., Bel, J., Franceschini,
888 G., and d'Ostiani, L. F.: Towards a GIS-based analysis of mountain environments
889 and populations, Food and Agriculture Organization, Rome, 26, 2003.
- 890 Hurst, D., Lin, J. C., Romashkin, P., Gerbig, C., Daube, B. C., Matross, D. M., Wofsy, S.
891 C., and Elkins, J. W.: Continuing emissions of restricted halocarbons in the USA
892 and Canada: Are they still globally significant?, *Journal of Geophysical Research*,
893 111, doi:10.1029/2005JD006785-doi:006710.001029/002005JD006785, 2006.
- 894 IPCC: Climate Change 2014: Synthesis Report. Contribution of Working Groups I, II
895 and III to the Fifth Assessment Report of the Intergovernmental Panel on Climate
896 Change IPCC, Geneva, Switzerland, 151 pp., 2014.
- 897 Jeong, S., Zhao, C., Andrews, A. E., Bianco, L., Wilczak, J. M., and Fischer, M. L.:
898 Seasonal variation of CH₄ emissions from central California, *Journal of*
899 *Geophysical Research: Atmospheres*, 117, n/a-n/a, 10.1029/2011JD016896, 2012.
- 900 Keeling, C. D., Bacastow, R. B., Bain-Bridge, A. E., Ekdahl, C. A., Guenther, P. R.,
901 Waterman, L. S., and Chin, J. F. S.: Atmospheric carbon dioxide variations at
902 Mauna Loa Observatory, Hawaii, *Tellus*, 28, 538-551, 1976.
- 903 Kellendorfer, J., Walker, W., Kirsch, K., Fiske, G., Bishop, J., Lapoint, L., Hoppus, M.,
904 and Westfall, J.: NACP Aboveground Biomass and Carbon Baseline Data, V.2
905 (NBCD 2000), U.S.A., 2000, in, ORNL Distributed Active Archive Center, 2013.
- 906 Kim, S. Y., Millet, D. B., Hu, L., Mohr, M. J., Griffis, T. J., Wen, D., Lin, J. C., Miller, S.
907 M., and Longo, M.: Constraints on carbon monoxide emissions based on tall tower
908 measurements in the U.S. Upper Midwest, *Environmental Science and Technology*,
909 47, 8316-8324, 2013.
- 910 Knowles, J. F.: Spatio-temporal patterns of soil respiration and the age of respired carbon
911 from high-elevation alpine tundra, Ph.D., Department of Geography, University of
912 Colorado, Boulder, Boulder, Colorado, USA, 119 pp., 2015.
- 913 Lang, R. E., Sarzynski, A., and Muro, M.: Mountain megas: America's newest
914 metropolitan places and a federal partnership to help them prosper, Brookings
915 Institute, Washington, D.C., 64, 2008.
- 916 Le Quéré, C., Moriarty, R., Andrew, R. M., Peters, G. P., Ciais, P., Friedlingstein, P.,
917 Jones, S. D., Sitch, S., Tans, P., Arneeth, A., Boden, T. A., Bopp, L., Bozec, Y.,
918 Canadell, J. G., Chini, L. P., Chevallier, F., Cosca, C. E., Harris, I., Hoppema, M.,
919 Houghton, R. A., House, J. I., Jain, A. K., Johannessen, T., Kato, E., Keeling, R. F.,
920 Kitidis, V., Klein Goldewijk, K., Koven, C., Landa, C. S., Landschützer, P., Lenton,
921 A., Lima, I. D., Marland, G., Mathis, J. T., Metzl, N., Nojiri, Y., Olsen, A., Ono, T.,
922 Peng, S., Peters, W., Pfeil, B., Poulter, B., Raupach, M. R., Regnier, P., Rödenbeck,
923 C., Saito, S., Salisbury, J. E., Schuster, U., Schwinger, J., Séférian, R.,
924 Segschneider, J., Steinhoff, T., Stocker, B. D., Sutton, A. J., Takahashi, T.,
925 Tilbrook, B., van der Werf, G. R., Viovy, N., Wang, Y. P., Wanninkhof, R.,
926 Wiltshire, A., and Zeng, N.: Global carbon budget 2014, *Earth Syst. Sci. Data*, 7,
927 47-85, 10.5194/essd-7-47-2015, 2015.
- 928 Levin, I., and Karstens, U. T. E.: Inferring high-resolution fossil fuel CO₂ records at
929 continental sites from combined 14CO₂ and CO observations, *Tellus B*, 59, 245-
930 250, 10.1111/j.1600-0889.2006.00244.x, 2007.



- 931 Lin, J. C., Gerbig, C., Wofsy, S. C., Andrews, A. E., Daube, B. C., Davis, K. J., and
932 Grainger, C. A.: A near-field tool for simulating the upstream influence of
933 atmospheric observations: the Stochastic Time-Inverted Lagrangian Transport
934 (STILT) model, *Journal of Geophysical Research*, 108, doi:10.1029/2002JD003161,
935 2003.
- 936 Lin, J. C., Gerbig, C., Wofsy, S. C., Andrews, A. E., Daube, B. C., Grainger, C. A., B.B,
937 S., Bakwin, P. S., and Hollinger, D. Y.: Measuring fluxes of trace gases at regional
938 scales by Lagrangian observations: application to the CO₂ Budget and Rectification
939 Airborne (COBRA) study, *Journal of Geophysical Research*, 109,
940 doi:10.1029/2004JD004754, doi:10.1029/2004JD004754, 2004.
- 941 Lin, J. C., and Gerbig, C.: Accounting for the effect of transport errors on tracer
942 inversions, *Geophysical Research Letters*, 32, doi:10.1029/2004GL021127-
943 doi:021110.021029/022004GL021127, 2005.
- 944 Lin, J. C.: Lagrangian modeling of the atmosphere: an introduction, in: *Lagrangian
945 Modeling of the Atmosphere*, edited by: Lin, J. C., Brunner, D., Gerbig, C., Stohl,
946 A., Luhar, A., and Webley, P., *Geophysical Monograph*, American Geophysical
947 Union, 1-11, 2012.
- 948 Lin, J. C., Brunner, D., Gerbig, C., Stohl, A., Luhar, A. K., and Webley, P. W.:
949 *Lagrangian Modeling of the Atmosphere*, in: *Geophysical Monograph*, American
950 Geophysical Union, 349, 2012.
- 951 Mallia, D. V., Lin, J. C., Urbanski, S., Ehleringer, J., and Nehrkorn, T.: Impacts of
952 upstream wildfire emissions on CO, CO₂, and PM_{2.5} concentrations in Salt Lake
953 City, Utah, *Journal of Geophysical Research*, 120, doi:10.1002/2014JD022472,
954 2015.
- 955 Mell, W. E., Manziello, S. L., Maranghides, A., Butry, D., and Rehm, R. G.: The
956 wildland-urban interface fire problem--current approaches and research needs,
957 *International Journal of Wildland Fire*, 19, 238-251, 2010.
- 958 Mitchell, L. E., Lin, J. C., Bowling, D. R., Pataki, D. E., Strong, C., Schauer, A. J., Bares,
959 R., Bush, S., Stephens, B. B., Mendoza, D., Mallia, D. V., Holland, L., Gurney, K.
960 R., and Ehleringer, J. R.: Long-term urban carbon dioxide observations reveal
961 spatial and temporal dynamics related to urban form and growth, *Proceedings of the
962 National Academy of Sciences*, In Review.
- 963 Monson, R. K., Turnipseed, A. A., Sparks, J. P., Harley, P. C., Scott-Denton, L. E.,
964 Sparks, K., and Huxman, T. E.: Carbon sequestration in a high-elevation, subalpine
965 forest, *Global Change Biology*, 8, 459-478, 2002.
- 966 Monson, R. K., Lipson, D. L., Burns, S. P., Turnipseed, A. A., Delany, A. C., Williams,
967 M. W., and Schmidt, S. K.: Winter forest soil respiration controlled by climate and
968 microbial community composition, *Nature*, 711-714, 2006.
- 969 Mu, M., Randerson, J. T., van der Werf, G. R., Giglio, L., Kasibhatla, P., Morton, D.,
970 Collatz, G. J., DeFries, R. S., Hyer, E. J., Prins, E. M., Griffith, D. W. T., Wunch,
971 D., Toon, G. C., Sherlock, V., and Wennberg, P. O.: Daily and 3-hourly variability
972 in global fire emissions and consequences for atmospheric model predictions of
973 carbon monoxide, *Journal of Geophysical Research-Atmospheres*, 116, 2011.
- 974 Negron, J. F., and Popp, J. B.: Probability of ponderosa pine infestation by mountain pine
975 beetle in the Colorado Front Range, *Forest Ecology and Management*, 191, 2004.



- 976 Nehr Korn, T., Eluszkiewicz, J., Wofsy, S. C., Lin, J. C., Gerbig, C., Longo, M., and
977 Freitas, S.: Coupled Weather Research and Forecasting–Stochastic Time-Inverted
978 Lagrangian Transport (WRF–STILT) model, *Meteorology and Atmospheric*
979 *Physics*, 107, 51-64, 2010.
- 980 Parrish, D. D., Hahn, C. H., Fahey, D. W., Williams, E. J., Bollinger, M. J., Hübler, G.,
981 Buhr, M. P., Murphy, P. C., Trainer, M., Hsie, E. Y., Liu, S. C., and Fehsenfeld, F.
982 C.: Systematic variations in the concentration of NO_x (NO Plus NO₂) at Niwot
983 Ridge, Colorado, *Journal of Geophysical Research: Atmospheres*, 95, 1817-1836,
984 10.1029/JD095iD02p01817, 1990.
- 985 Peters, W., Jacobson, A., Sweeney, C., Andrews, A. E., Conway, T. J., Masarie, K. A.,
986 Miller, J. B., Bruhwiler, L., Petron, G., Hirsch, A. I., Worthy, D., van der Werf, G.
987 R., Randerson, J. T., Wennberg, P. O., Krol, M. C., and Tans, P. P.: An
988 atmospheric perspective on North American carbon dioxide exchange:
989 CarbonTracker, *Proceedings of the National Academy of Sciences*, 104, 18925-
990 18930, 2007.
- 991 Peters, W., Krol, M. C., Van Der Werf, G. R., Houweling, S., Jones, C. D., Hughes, J.,
992 Schaefer, K., Masarie, K. A., Jacobson, A. R., Miller, J. B., Cho, C. H., Ramonet,
993 M., Schmidt, M., Ciattaglia, L., Apadula, F., Heltai, D., Meinhardt, F., Di Sarra, A.
994 G., Piacentino, S., Sferlazzo, D., Aalto, T., Hatakka, J., Ström, J., Haszpra, L.,
995 Meijer, H. A. J., Van Der Laan, S., Neubert, R. E. M., Jordan, A., Rodó, X.,
996 Morguí, J. A., Vermeulen, A. T., Popa, E., Rozanski, K., Zimnoch, M., Manning, A.
997 C., Leuenberger, M., Uglietti, C., Dolman, A. J., Ciais, P., Heimann, M., and Tans,
998 P. P.: Seven years of recent European net terrestrial carbon dioxide exchange
999 constrained by atmospheric observations, *Global Change Biology*, 16, 1317-1337,
1000 10.1111/j.1365-2486.2009.02078.x, 2010.
- 1001 Pillai, D., Gerbig, C., Ahmadov, R., Rodenbeck, C., Kretschmer, R., Koch, T., Thompson,
1002 R., Neininger, B., and Lavrie, J. V.: High-resolution simulations of atmospheric
1003 CO₂ over complex terrain – representing the Ochsenkopf mountain tall tower,
1004 *Atmospheric Chemistry and Physics*, 11, 7445-7464, 2011.
- 1005 Potter, C., Fladland, M., Klooster, S., Genovese, V., Hiatt, S., and Gross, P.: Satellite
1006 Data Analysis and Ecosystem Modeling for Carbon Sequestration Assessments in
1007 the Western United States, in: *Carbon Sequestration and Its Role in the Global*
1008 *Carbon Cycle*, American Geophysical Union, 89-99, 2013.
- 1009 Ramankutty, N., and Foley, J. A.: Estimating historical changes in global land cover:
1010 Croplands from 1700 to 1992, *Global Biogeochemical Cycles*, 13, 997-1027,
1011 10.1029/1999GB900046, 1999.
- 1012 Reisner, M.: Cadillac desert: The American West and its disappearing water, Penguin,
1013 1993.
- 1014 Rinsland, C. P., Mahieu, E., Zander, R., Demoulin, P., Forrer, J., and Buchmann, B.: Free
1015 tropospheric CO, C₂H₆, and HCN above central Europe: Recent measurements
1016 from the Jungfraujoch station including the detection of elevated columns during
1017 1998, *Journal of Geophysical Research: Atmospheres*, 105, 24235-24249,
1018 10.1029/2000JD900371, 2000.
- 1019 Rodenbeck, C.: Estimating CO₂ sources and sinks from atmospheric mixing ratio
1020 measurements using a global inversion of atmospheric transport, *Max-Planck*
1021 *Institut für Biogeochemie, Jena, Germany*, 53, 2005.



- 1022 Rotach, M. W., Andretta, M., Calanca, P., Weigel, A. P., and Weiss, A.: Boundary layer
1023 characteristics and turbulent exchange mechanisms in highly complex terrain, *Acta*
1024 *Geophysica*, 56, 194-219, 2008.
- 1025 Rotach, M. W., Wohlfahrt, G., Hansel, A., Reif, M., Wagner, J., and Gohm, A.: The
1026 world is not flat: implications for the global carbon balance, *Bulletin of the*
1027 *American Meteorological Society*, 95, 1021-1028, 2014.
- 1028 Sarmiento, J. L., Gloor, M., Gruber, N., Beaulieu, C., Jacobson, A. R., Mikaloff-Fletcher,
1029 S. E., Pacala, S., and Rodgers, K.: Trends and regional distributions of land and
1030 ocean carbon sinks, *Biogeosciences*, 7, 2351-2367, 2010.
- 1031 Schimel, D., Running, S., Monson, R., Turnipseed, A., and Anderson, D.: Carbon
1032 sequestration in the mountains of the Western US, *Eos*, 83, 445-456, 2002.
- 1033 Schmidt, M., Graul, R., Sartorius, H., and Levin, I.: The Schauinsland CO₂ record: 30
1034 years of continental observations and their implications for the variability of the
1035 European CO₂ budget, *Journal of Geophysical Research: Atmospheres*, 108, n/a-
1036 n/a, 10.1029/2002jd003085, 2003.
- 1037 Schwalm, C. R., Williams, C. A., Schaefer, K., Baldocchi, D., Black, T. A., Goldstein, A.
1038 H., Law, B. E., Oechel, W. C., Paw U, K. T., and Scott, R. L.: Reduction in carbon
1039 uptake during turn of the century drought in western North America, *Nature*
1040 *Geoscience*, doi:10.1038/NNGEO1529, 2012.
- 1041 Skamarock, W. C., and Klemp, J. B.: A time-split nonhydrostatic atmospheric model for
1042 weather research and forecasting applications, *Journal of Computational Physics*,
1043 227, 3465-3485, 2008.
- 1044 Stephens, B. B., Gurney, K. R., Tans, P. P., Sweeney, C., Peters, W., Bruhwiler, L., Ciais,
1045 P., Ramonet, M., Bousquet, P., and Nakazawa, T.: Weak northern and strong
1046 tropical land carbon uptake from vertical profiles of atmospheric CO₂, *Science*, 316,
1047 1732-1735, 2007.
- 1048 Stephens, B. B., Miles, N. L., Richardson, S. J., Watt, A. S., and Davis, K. J.:
1049 Atmospheric CO₂ monitoring with single-cell NDIR-based analyzers, *Atmospheric*
1050 *Measurement Techniques*, 4, 2737-2748, 2011.
- 1051 Steyn, D., De Wekker, S. J., Kossmann, M., and Martilli, A.: Boundary Layers and Air
1052 Quality in Mountainous Terrain, in: *Mountain Weather Research and Forecasting*,
1053 edited by: Chow, F. K., De Wekker, S. F. J., and Snyder, B. J., Springer
1054 *Atmospheric Sciences*, Springer Netherlands, 261-289, 2013.
- 1055 Sun, J., Burns, S. P., Delany, A. C., Oncley, S. P., Turnipseed, A. A., Stephens, B. B.,
1056 Lenschow, D. H., LeMone, M. A., Monson, R. K., and Anderson, D. E.: CO₂
1057 transport over complex terrain, *Agricultural and Forest Meteorology*, 145, 1-21,
1058 <http://dx.doi.org/10.1016/j.agrformet.2007.02.007>, 2007.
- 1059 Sun, J., Oncley, S. P., Burns, S. P., Stephens, B. B., Lenschow, D. H., Campos, T.,
1060 Monson, R. K., Schimel, D. S., Sacks, W. J., De Wekker, S. F. J., Lai, C. T., Lamb,
1061 B., Ojima, D., Ellsworth, P. Z., Sternberg, L. S. L., Zhong, S., Clements, C., Moore,
1062 D. J. P., Anderson, D. E., Watt, A. S., Hu, J., Tschudi, M., Aulenbach, S., Allwine,
1063 E., and Coons, T.: A multiscale and multidisciplinary investigation of ecosystem-
1064 atmosphere CO₂ exchange over the Rocky Mountains of Colorado, *Bulletin of the*
1065 *American Meteorological Society*, 209-230, 2010.



- 1066 Sun, J., and De Wekker, S. F. J.: Atmospheric carbon dioxide transport over mountainous
1067 terrain, in: Mountain Ecosystems, edited by: Richards, K. E., Nova Science
1068 Publishers, 101-121, 2011.
- 1069 Tkacz, B., Moody, B., Castillo, J. V., and Fenn, M. E.: Forest health conditions in North
1070 America, Environmental Pollution, 155, 409-425,
1071 <http://dx.doi.org/10.1016/j.envpol.2008.03.003>, 2008.
- 1072 Tuzson, B., Henne, S., Brunner, D., Steinbacher, M., Mohn, J., Buchmann, B., and
1073 Emmenegger, L.: Continuous isotopic composition measurements of tropospheric
1074 CO₂ at Jungfrauoch (3580 m a.s.l.), Switzerland: real-time observation of regional
1075 pollution events, Atmos. Chem. Phys., 11, 1685-1696, 10.5194/acp-11-1685-2011,
1076 2011.
- 1077 Urbanski, S. P., Hao, W. M., and Nordgren, B.: The wildland fire emission inventory:
1078 western United States emission estimates and an evaluation of uncertainty,
1079 Atmospheric Chemistry and Physics, 11, 12973-13000, 2011.
- 1080 van der Molen, M. K., and Dolman, A. J.: Regional carbon fluxes and the effect of
1081 topography on the variability of atmospheric CO₂, Journal of Geophysical
1082 Research: Atmospheres, 112, n/a-n/a, 10.1029/2006JD007649, 2007.
- 1083 van der Werf, G. R., Randerson, J. T., Giglio, L., Collatz, G. J., Mu, M., Kasibhatla, P. S.,
1084 Morton, D. C., DeFries, R. S., Jin, Y., and van Leeuwen, T. T.: Global fire
1085 emissions, and the contribution of deforestation, savanna, forest, agricultural, and
1086 peat fires (1997-2009), Atmospheric Chemistry and Physics, 10, 11707-11735,
1087 2010.
- 1088 Wharton, S., Falk, M., Bible, K., Schroeder, M., and Paw U, K. T.: Old-growth CO₂ flux
1089 measurements reveal high sensitivity to climate anomalies across seasonal, annual
1090 and decadal time scales, Agricultural and Forest Meteorology, 161, 1-14, 2012.
- 1091 Wiedinmyer, C., and Neff, J. C.: Estimates of CO₂ from fires in the United States:
1092 implications for carbon management, Carbon Balance and Management, 2,
1093 10.1186/1750-0680-2-10, 2007.
- 1094 Yi, C., Anderson, D. E., Turnipseed, A. A., Burns, S. P., Sparks, J. P., Stannard, D. I.,
1095 and Monson, R. K.: The contribution of advective fluxes to net ecosystem CO₂
1096 exchange in a high-elevation, subalpine forest, Ecological Applications, 18, 1379-
1097 1390, 2008.
- 1098 Zardi, D., and Whiteman, C. D.: Diurnal Mountain Wind Systems, in: Mountain Weather
1099 Research and Forecasting, edited by: Chow, F. K., De Wekker, S. F. J., and Snyder,
1100 B. J., Springer Atmospheric Sciences, Springer Netherlands, 35-119, 2013.
- 1101
1102



Above-ground Biomass in the Western U.S.

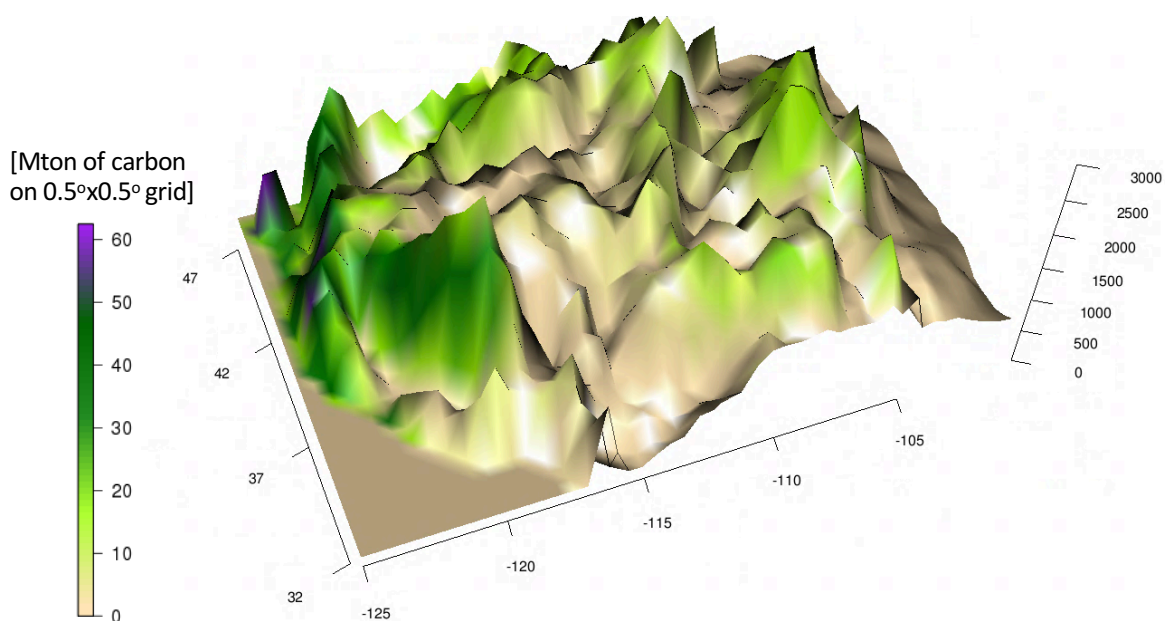


Fig. 1



WRF Domains

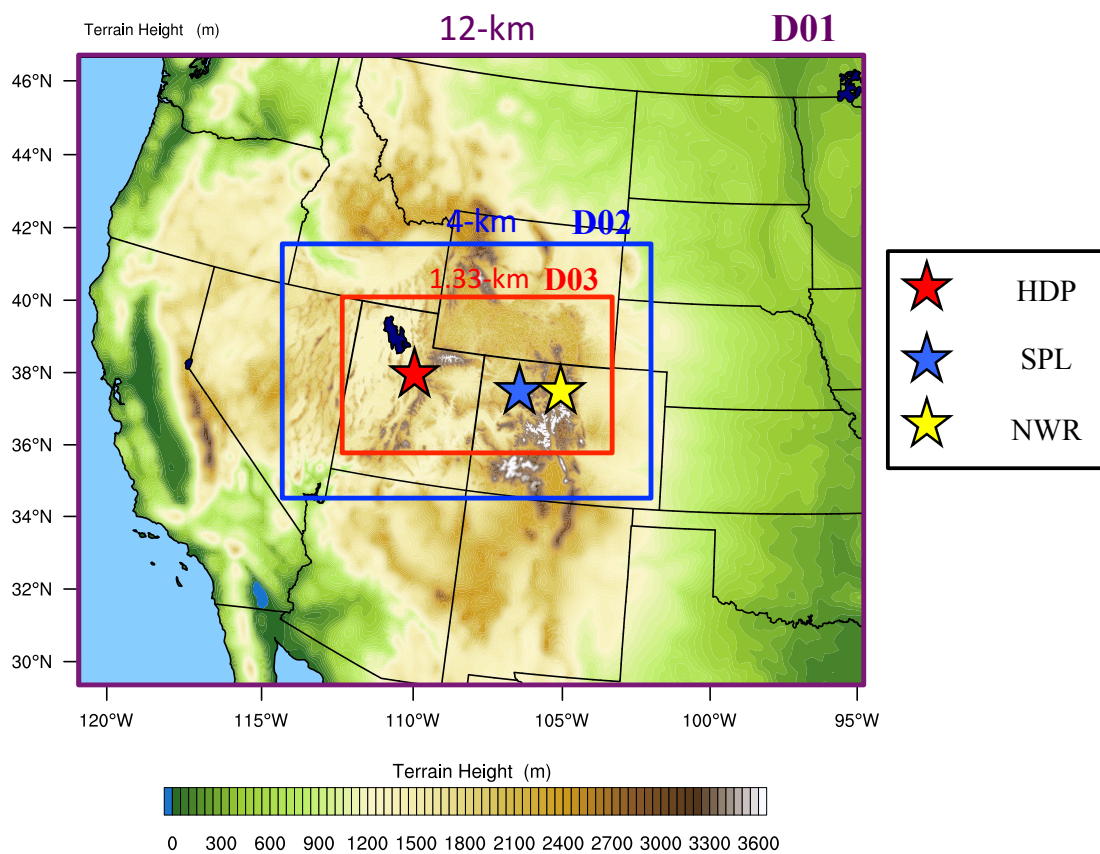


Fig. 2

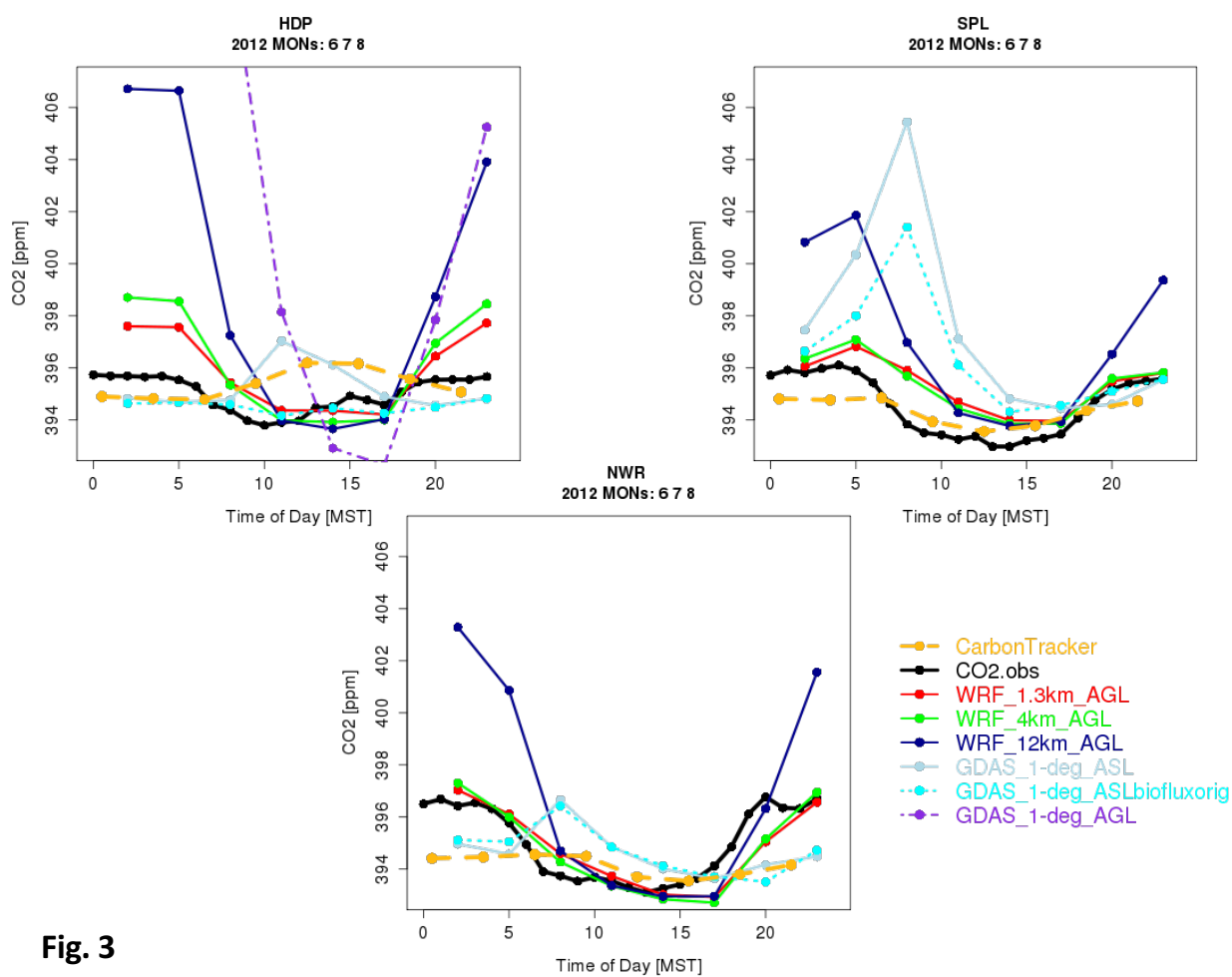


Fig. 3

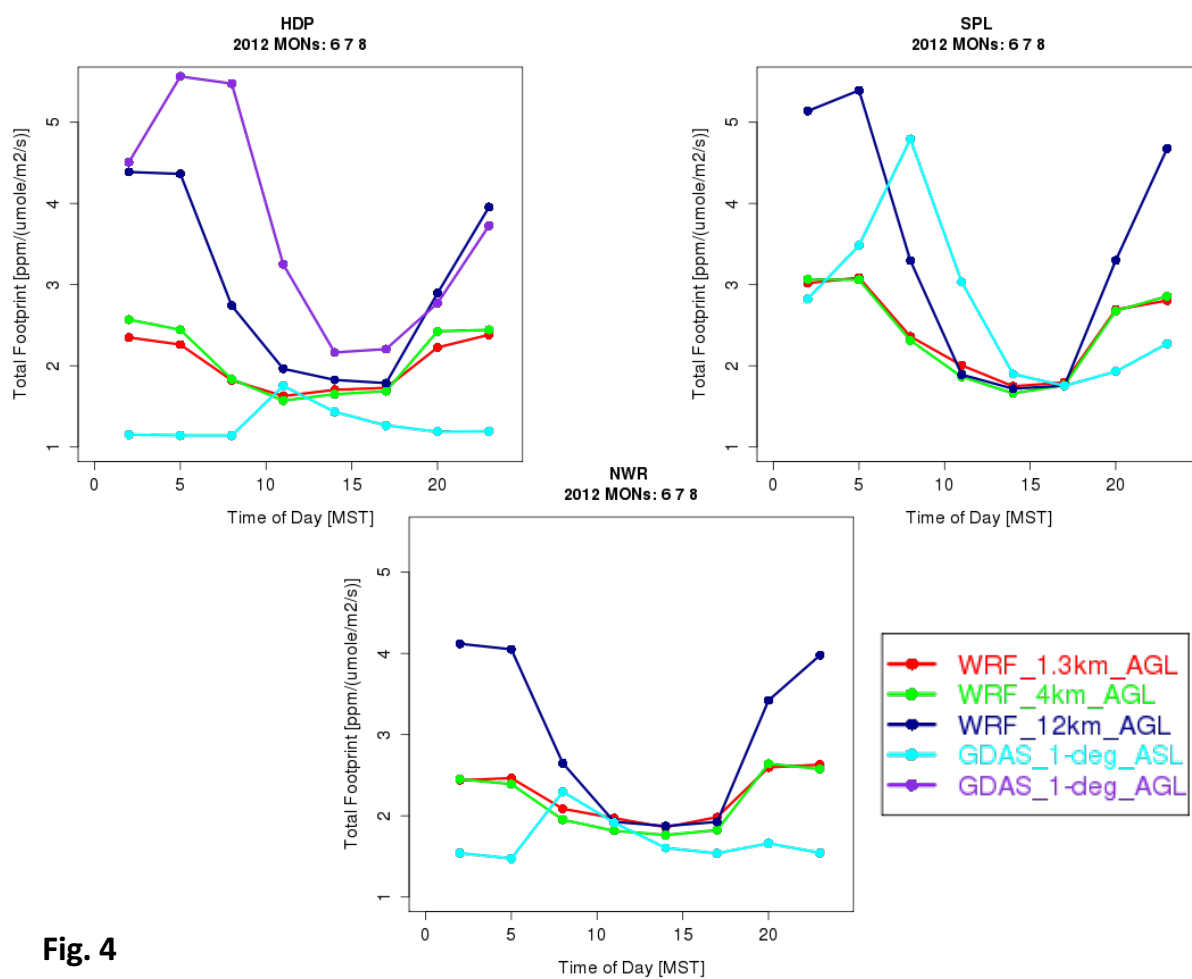


Fig. 4

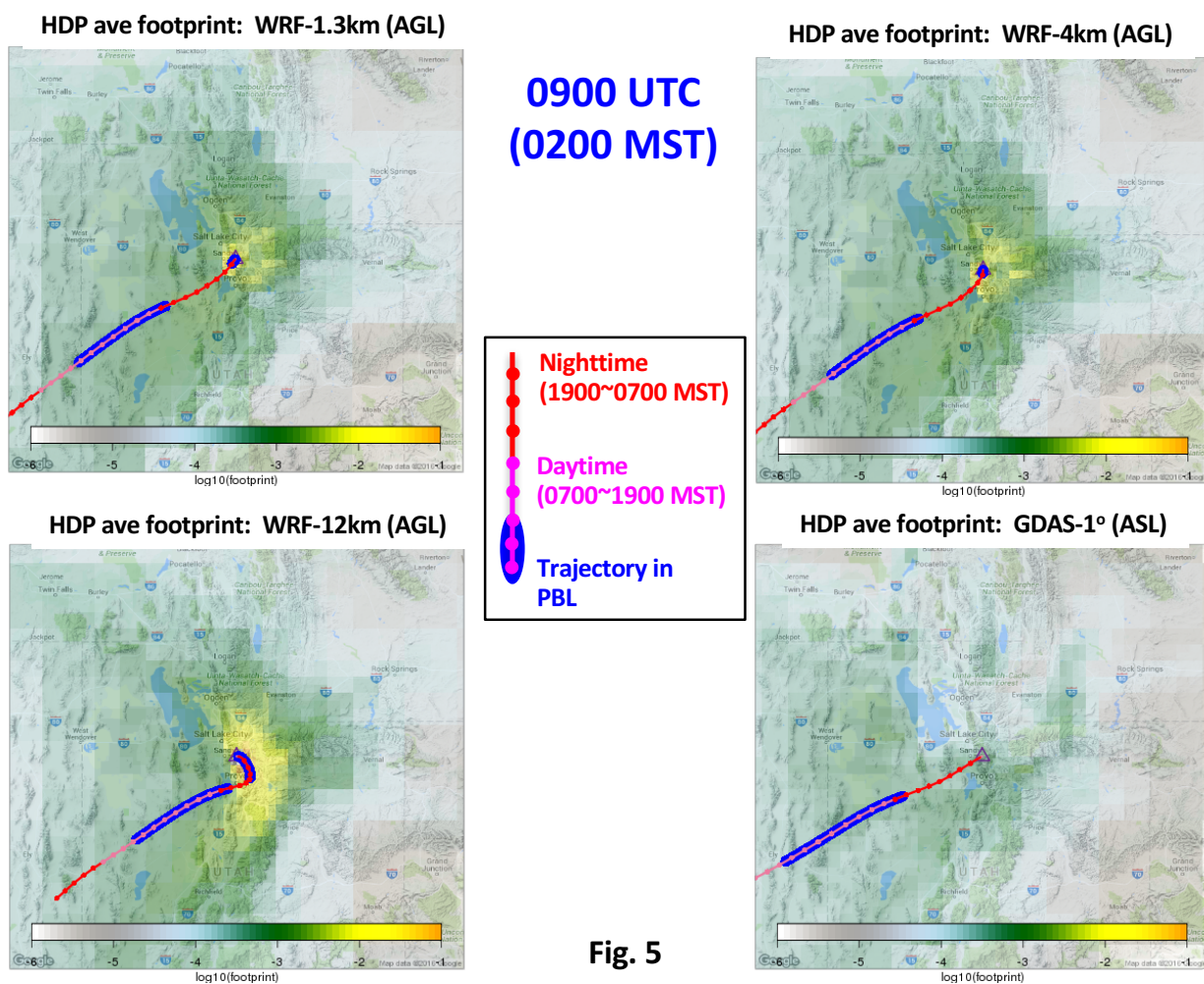


Fig. 5

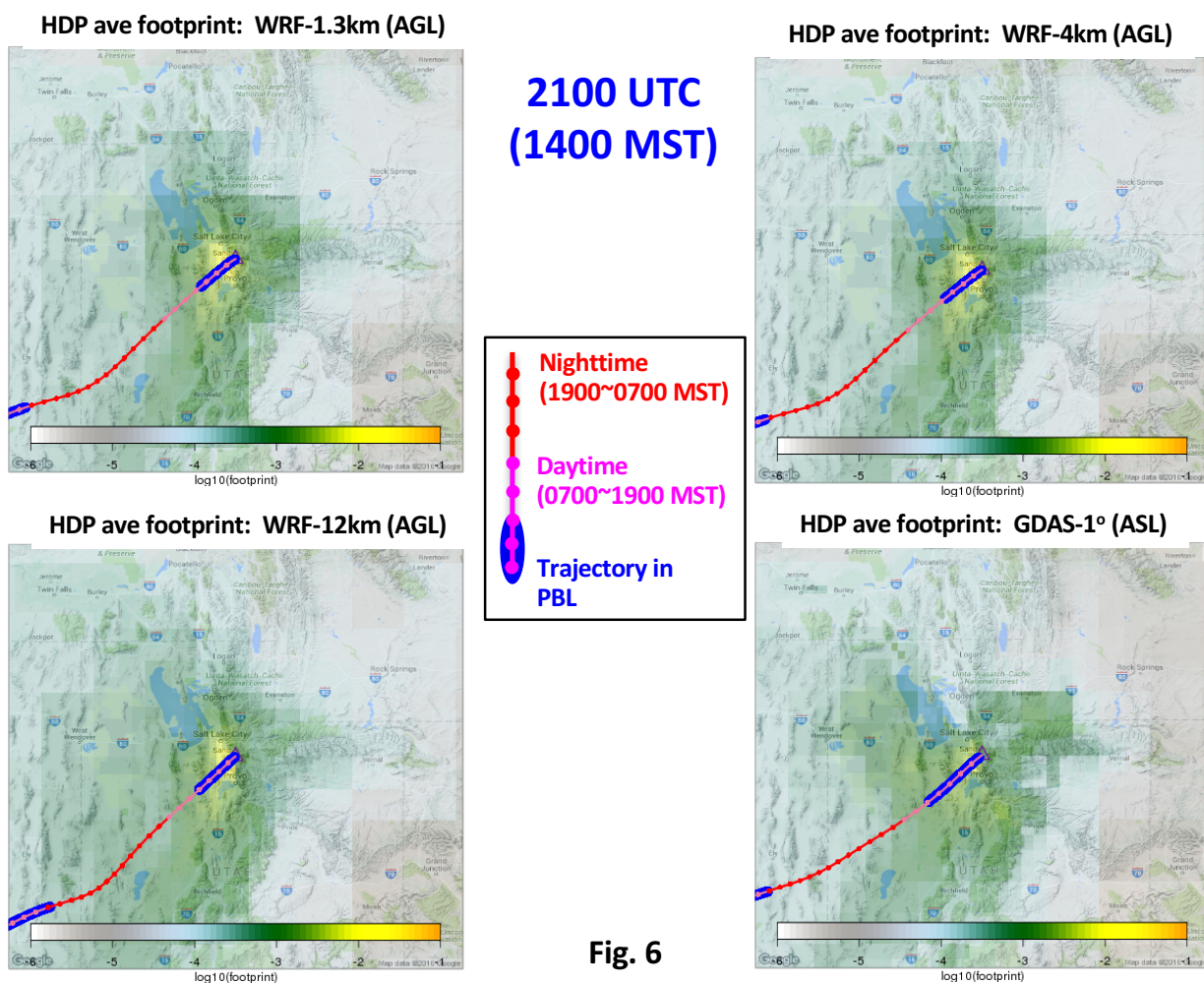


Fig. 6



HDP: Mean 3D Trajectory of Stochastic Particles & PBL ht for Different Runs 0900 UTC (0200 MST)

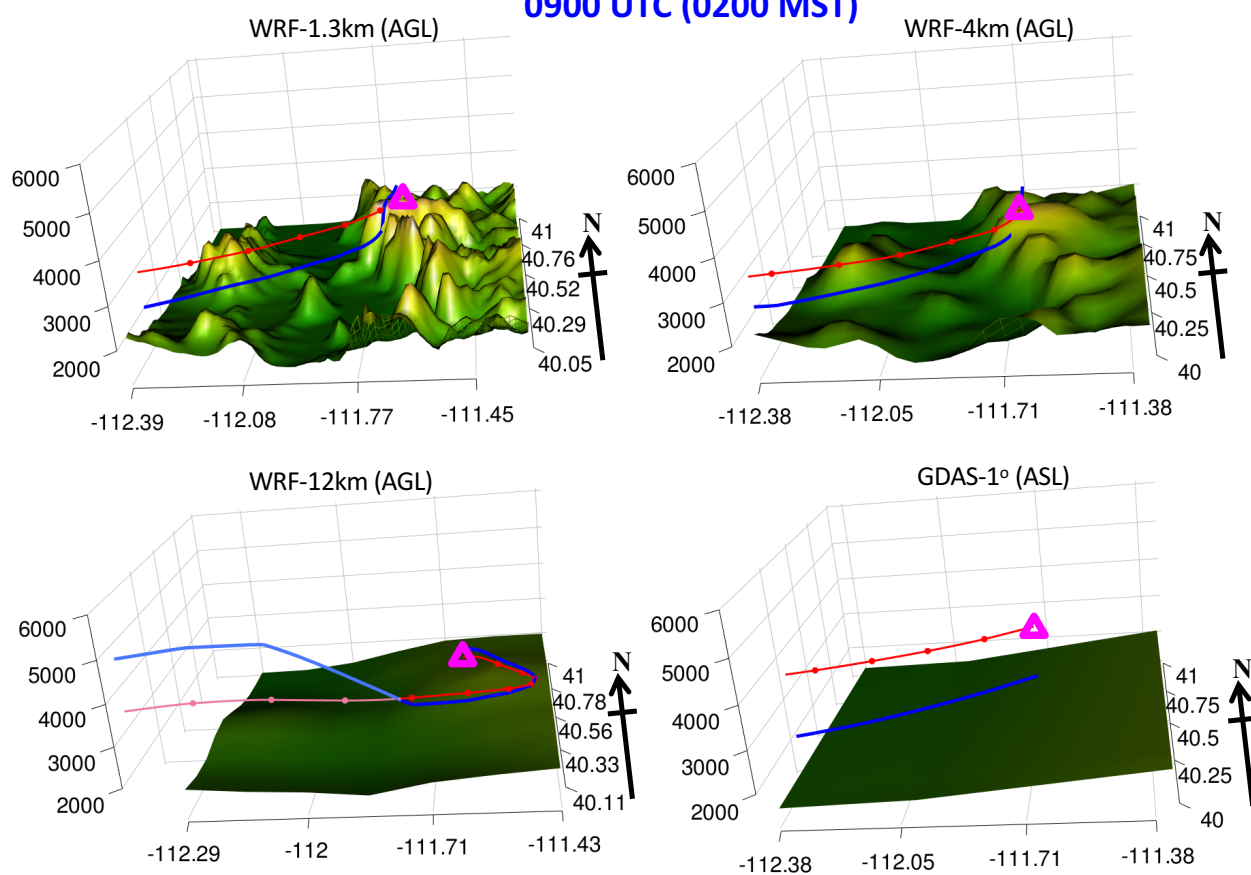


Fig. 7



HDP: Mean 3D Trajectory of Stochastic Particles & PBL ht (above ground level)

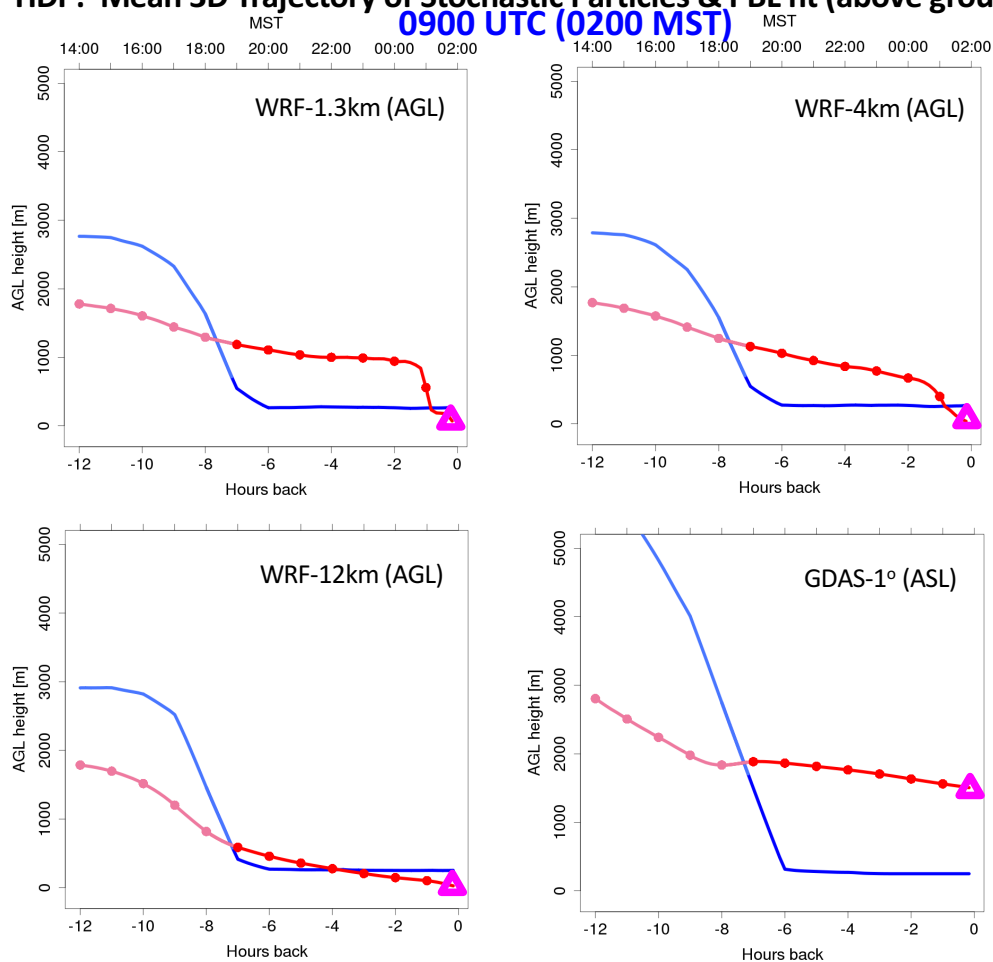
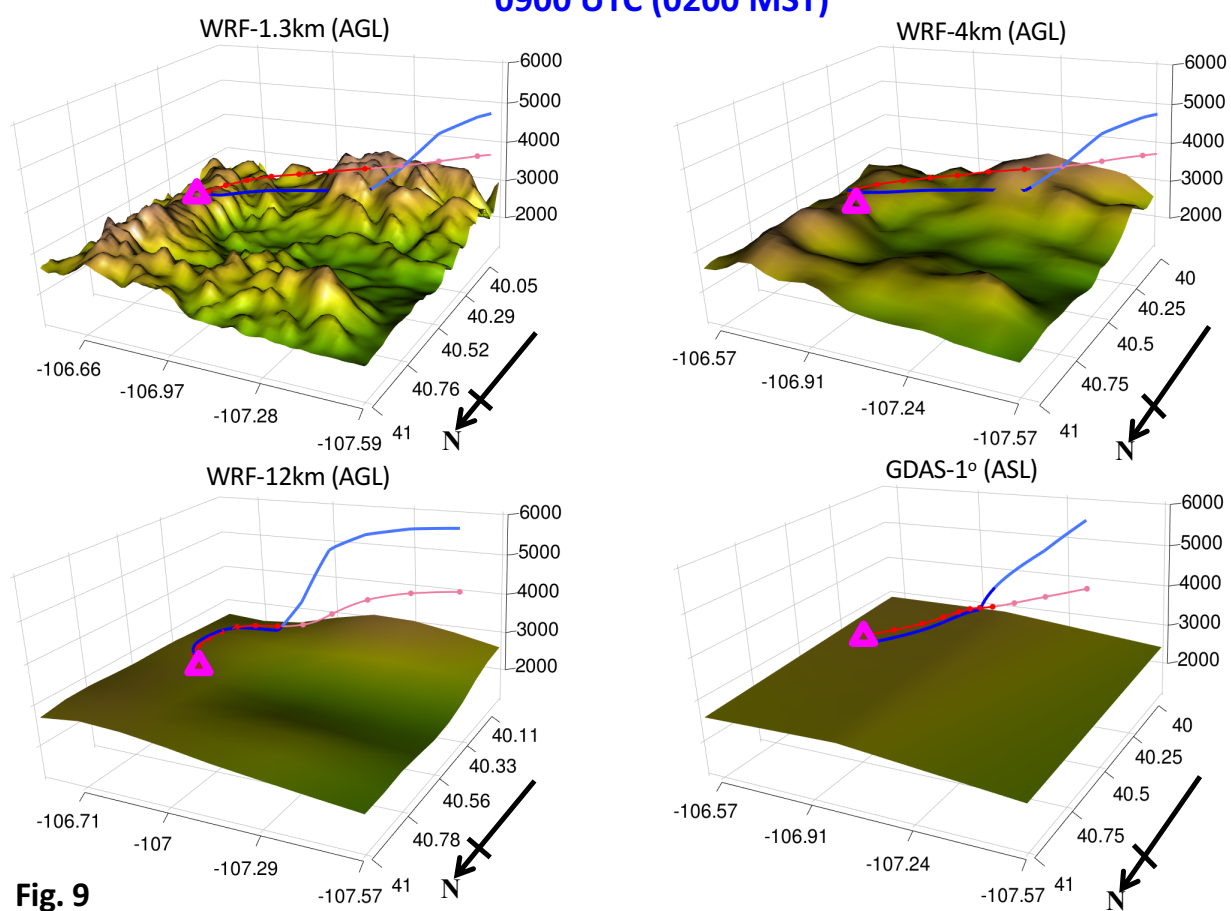


Fig. 8



SPL: Mean 3D Trajectory of Stochastic Particles & PBL ht for Different Runs 0900 UTC (0200 MST)





SPL: Mean 3D Trajectory of Stochastic Particles & PBL ht (above ground level)

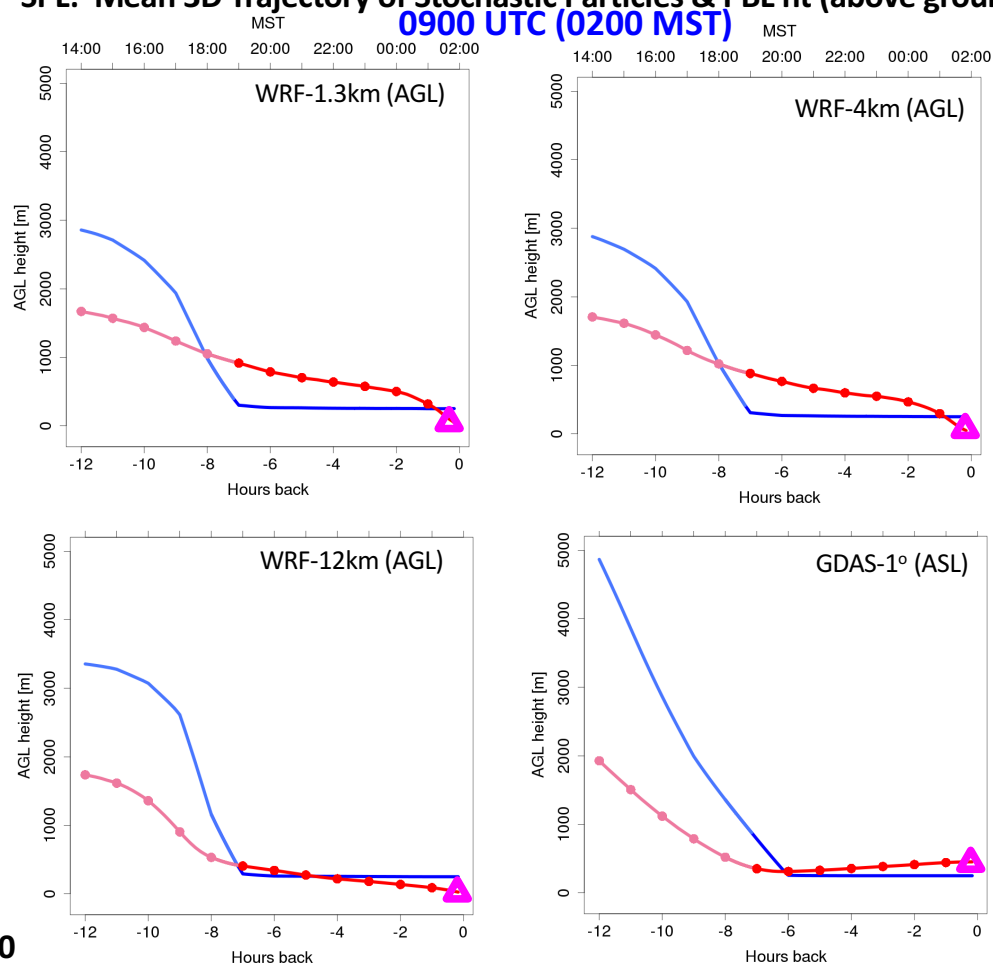


Fig. 10



NWR: Mean 3D Trajectory of Stochastic Particles & PBL ht for Different Runs
0900 UTC (0200 MST)

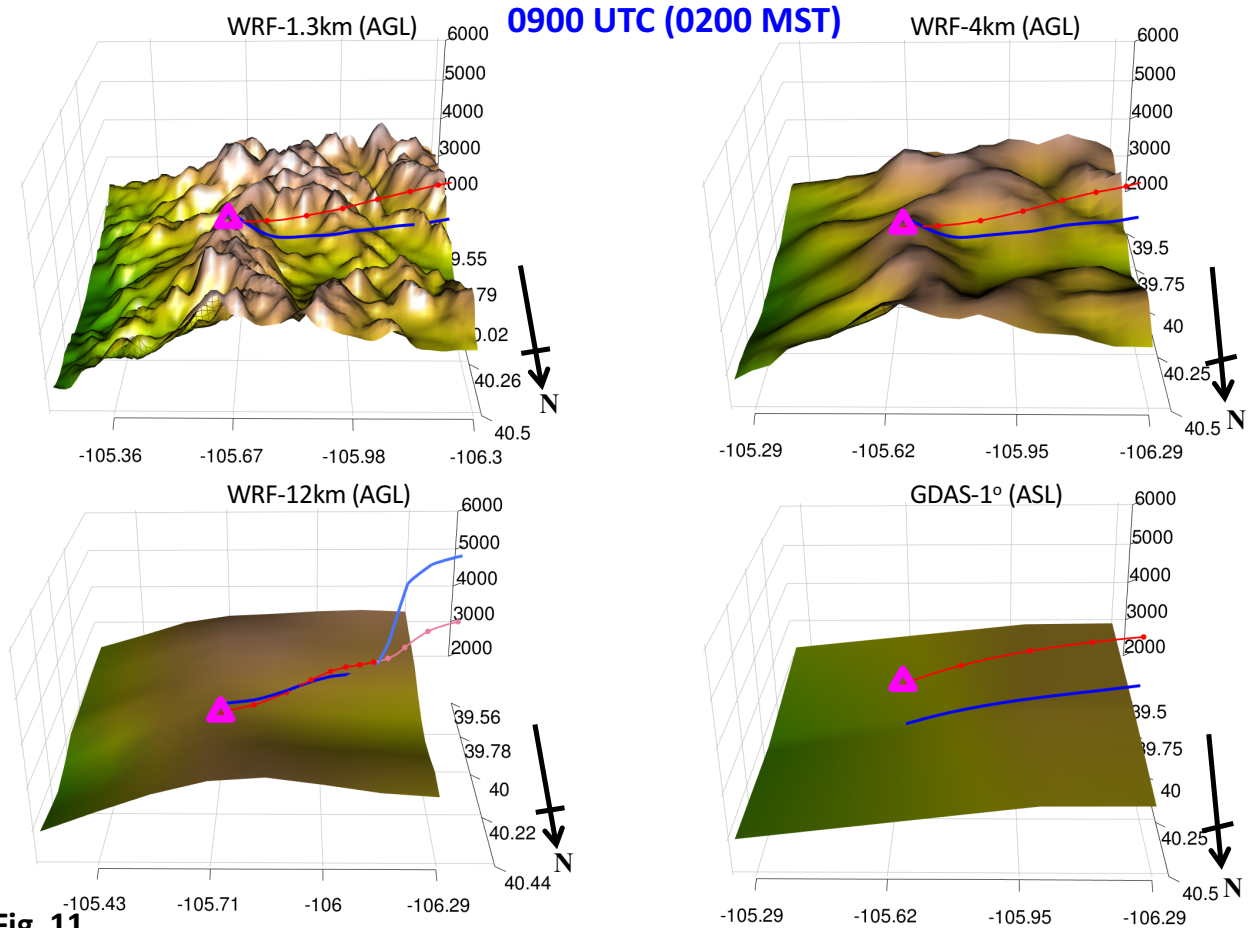


Fig. 11



NWR: Mean 3D Trajectory of Stochastic Particles & PBL ht (above ground level)

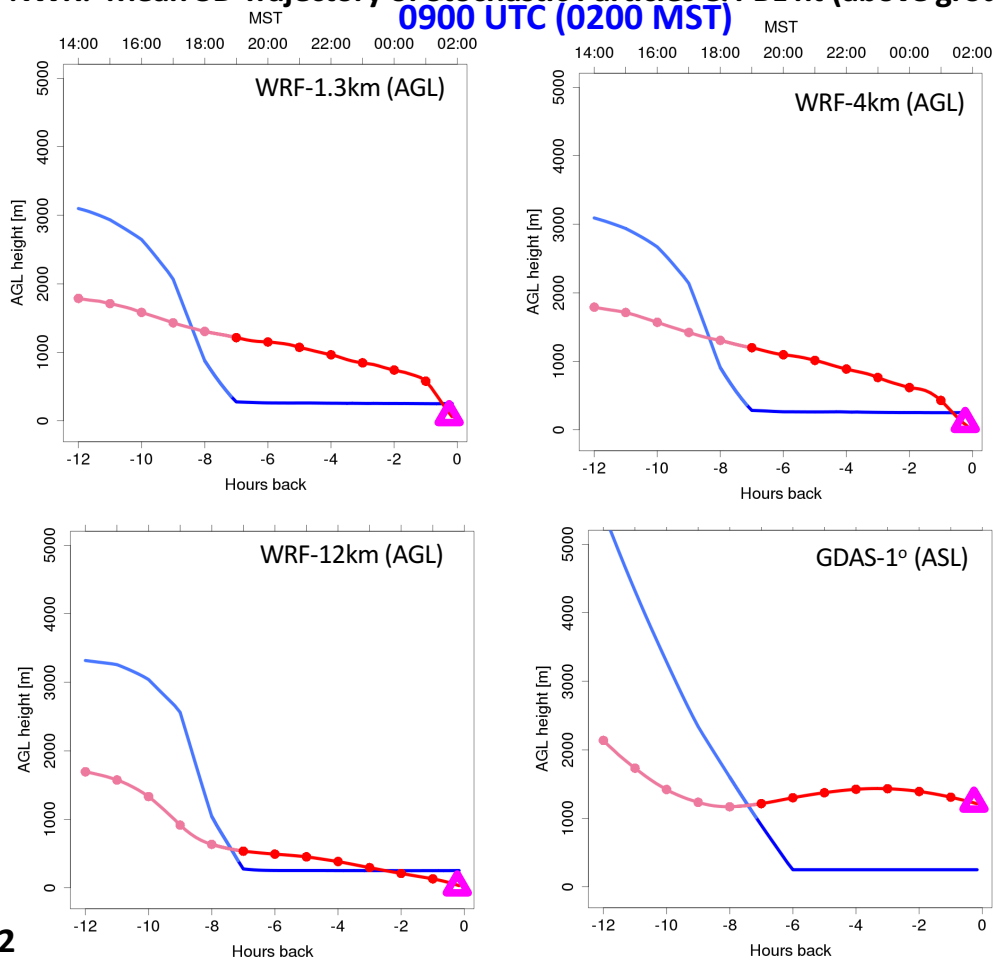


Fig. 12



Mean 3D Trajectory of Stochastic Particles & PBL ht GDAS-1° (ASL)

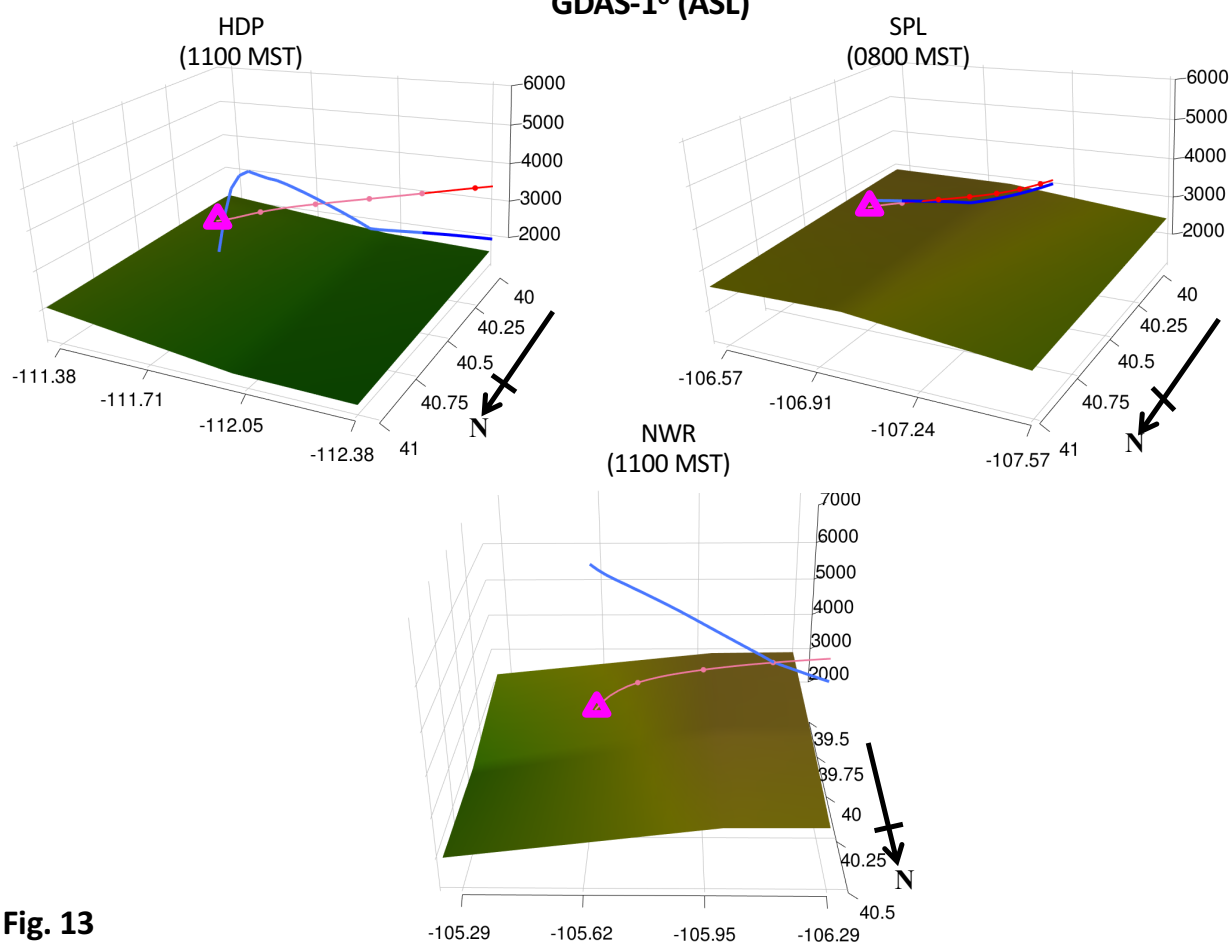


Fig. 13